BNL-106289-2014-JA

Interactions between Cumulus Convection and Its Environment as Revealed by the MC3E Sounding Array

Shaocheng Xie[1], Yunyan Zhang[1], Scott E. Giangrande[2], Michael P. Jensen[2], Renata McCoy[1], Minghua Zhang[3]

[1]Lawrence Livermore National Laboratory, Livermore, California, USA
[2]Brookhaven National Laboratory, Upton, New York, USA
[3]Stony Brook University, Stony Brook, NY, USA

Corresponding author: Shaocheng Xie

Email: xie2@llnl.gov

Phone: 925-422-6023

Fax: 925-422-7675

Accepted Article

This article has been accepted for publication and undergone full peer review but has not been through the copyediting, typesetting, pagination and proofreading process which may lead to differences between this version and the Version of Record. Please cite this article as doi: 10.1002/2014JD022011

Abstract

This study attempts to understand interactions between midlatitude convective systems and their environments through a heat and moisture budget analysis using the sounding data collected from the Midlatitude Continental Convective Clouds Experiment (MC3E) in central Oklahoma. Distinct large-scale structures and diabatic heating and drying profiles are presented for cases of weaker and elevated thunderstorms as well as intense squall line and supercell thunderstorm events during the campaign. The elevated cell events were nocturnal convective systems occurring in an environment having low CAPE and a very dry boundary layer. In contrast, deeper convective events happened during the morning into early afternoon within an environment associated with large CAPE and a near-saturated boundary layer. As the systems reached maturity, the diagnosed diabatic heating in the latter deep convective cases was much stronger and of greater vertical extent than the former. Both groups showed considerable diabatic cooling in the lower troposphere, associated with the evaporation of precipitation and low-level clouds. The horizontal advection of moisture also played a dominant role in moistening the lower troposphere, particularly for the deeper convective events, wherein the near surface south-easterly flow allows persistent low-level moisture return from the Gulf of Mexico to support convection. The moisture convergence often was present before these systems develop, suggesting a strong correlation between the large-scale moisture convergence and convection. Sensitivity tests indicated that the uncertainty in the surface precipitation and the size of analysis domain mainly affected the magnitude of these analyzed fields rather than their vertical structures.

Accepted Article

1. Introduction

After decades of effort, accurately representing cumulus convection is still one of the most challenging tasks for weather and climate modeling. This is primarily because the interaction between cumulus convection and its environment has not been fully understood. In general, the large-scale state of the atmosphere, as characterized by low-level convergence and moistening and middle and upper level advective cooling, acts to destabilize the atmospheric structure, thereby initiating and maintaining convection. On the other hand, cumulus clouds modify the temperature and moisture structure of the environment through the release of latent heat and the vertical redistribution of sensible heat and water vapor [Riehl and Malkus, 1958; Yanai, 1961; Yanai and Johnson, 1993]. However, the details of these interactions may differ, depending on the large-scale conditions and vertical structures of diabatic heating and drying. These interactions also may vary according to the temporal and spatial scales of interest.

Collecting the observational data necessary to diagnose vertical structures of latent heating and the drying associated with convective systems has been a primary goal for numerous major field experiments [e.g., Webster and Lukas, 1992; May et al., 2008; Zhang et al., 2013]. During convective periods, latent heating is the dominant component of total diabatic heating. The total diabatic heating and drying, jointly termed as the apparent heat source ($Q1$) and apparent moisture sink ($Q2$) according to Yanai et al. [1973], can be estimated as the residual of heat and moisture budgets of large-scale motion measured by a suitably designed sounding network [e.g., Yanai et al., 1973; Thompson et al., 1979; Ooyama, 1987; Zhang and Lin, 1997]. Previous budget diagnostic studies have often targeted tropical convective systems given the dominant role these convective systems play in the global water cycle [Thompson et al., 1979; Frank, 1978; Frank and McBride, 1989; Lin and

Accepted Article

Johnson, 1996a, b; and Schumacher et al., 2007; Xie et al., 2010a; Johnson and Ciesielski, 2013]. Few suitably designed field studies have been carried out in the midlatitudes [Ninomiya, 1971; Lewis, 1975; Kuo and Anthes, 1984; Gallus and Johnson, 1995; Hopper and Schumacher 2009, 2012].

Convection in the midlatitudes often occurs less frequent as compared to tropical counterparts. The low frequency of mid-latitude convective events implies that the overall impact of diabatic heating to the large scale environment is small compared to the tropics, but to the maintenance of the storms itself, it may be important. For example, the strong cooling due to drier lower troposphere will create stronger cold pools, which will have feedbacks to the storm (especially squall line) to sustain itself while propagating. In addition, groups of mesoscale convective systems (MCSs) that often occur in the midlatitude over a several-day period in the summer can have large impact on the large-scale flow patterns [Stensrud, 1996]. To provide a more comprehensive dataset to better characterize convection and its environment in the midlatitudes, a major field campaign - the Midlatitude Continental Convective Clouds Experiment (MC3E) [Jensen et al., 2010] was recently conducted from 22 April – 6 June 2011 at the Atmospheric Radiation Measurement (ARM) Southern Great Plains (SGP) site in central Oklahoma. This campaign was funded through a collaborative effect between the U. S. Department of Energy (DOE) ARM program and the National Aeronautic and Space Administration's (NASA) Global Precipitation Measurement (GPM) mission Ground Validation (GV) program. It leveraged the largest observing infrastructure currently available in the central United States to observe the detailed evolution of convective cloud systems and their large-scale conditions. A key component for this experiment included extensive radiosonde launches at 3-6 hour intervals over a distributed network of 6 sounding stations to capture the diurnal variability of convective cloud systems whenever they propagated over the SGP site. The dataset collected from this experiment and anchored by

Accepted Article

this extensive sounding array provided a unique opportunity to study the structure and evolution of these midlatitude convective systems and their associated environments at an unprecedented level of detail.

The goal of this study is to improve our understanding on the interactions between cumulus convection and its environment in midlatitude convective cloud systems using the unique data collected during MC3E. We include a comparison of well-organized squall lines and deeper convective systems with nocturnal weaker and elevated convective episodes over the ARM SGP location during the campaign. These are two typical convective systems that are often observed in this region. Using these unique MC3E sounding data constrained with surface and Top-Of-the-Atmosphere (TOA) measurements through a variational analysis method, we compute the large-scale budgets of temperature and moisture, then estimate the total diabatic heating and drying structures in these convective systems. Our focus is to define similarities and variations in large-scale conditions as well as diabatic heating and drying structures for the two different bulk convective cloud system types. We attempt to understand how the large-scale atmospheric structure interacts with these convective systems under different conditions. An important end product of this study is the analyzed large-scale vertical velocity and advective tendencies of temperature and moisture, which can be used to drive single-column models (SCMs) and cloud-resolving models (CRMs) for modeling study of these observed MC3E cloud systems [e.g., Ghan et al., 2000; Xie et al., 2002, 2005; Xu et al. 2002, 2005].

Details about the objective analysis method used in the budget analysis are provided in Section 2. Section 3 presents an overview of the observed convective systems and their environments. The analyzed heat and moisture budgets are discussed in Section 4. The discussion focuses on the similarities and differences in the budget terms and their large-scale structures between the examined weaker discrete and/or elevated thunderstorms and the

Accepted Article

intense squall line and supercell events. Section 5 analyzes impacts of uncertainties in the surface precipitation on the derived heat and moisture budgets, as well as how the heat and moisture budgets vary with different analysis domain sizes. Section 6 provides a summary of the study.

2. Analysis method

The method used to compute heat and moisture budgets is the constrained objective variational analysis approach of Zhang and Lin [1997]. This method was designed for deriving the large-scale vertical velocity and advective tendencies of temperature and moisture, the so-called large-scale forcing, from sounding measurements over a network with a small number of stations. Compared to other conventional objective analysis methods, the unique feature of the variational analysis is the use of domain-averaged surface and TOA observations as constraints to adjust atmospheric state variables from soundings by the smallest possible amount to conserve column-integrated mass, moisture, and static energy so that the final analysis data set is dynamically and thermodynamically consistent. The required observational constraints include the surface and TOA radiative fluxes, surface latent and sensible heat fluxes, and surface precipitation. This method has been successfully used to process data collected in major ARM field campaigns at its permanent research sites, such as the Oklahoma SGP site [Zhang et al., 2001], the North Slope of Alaska site [Xie et al., 2006], and the Tropical Western Pacific – Darwin site [Xie et al., 2010a]. It was also used for analyzing data from the Tropical Rainfall Measuring Mission (TRMM) Kwajalein Experiment (KWAJEX), the TRMM Large-Scale Biosphere-Atmosphere Experiment (LBA), and the TRMM South China Sea Monsoon Experiment (SCSMEX) [Schumacher et al., 2007]. In this section, we provide some technical details about the objective analysis of the MC3E observations.

Accepted Article

The MC3E sounding array consists of five sounding stations centered on a sixth site at the ARM SGP central facility (CF) (Fig. 1a). The sounding array covers an area with a diameter of approximately 300 km. The variational analysis technique described above was applied to MC3E over a domain that contains the five boundary sounding stations S01-S05 (Domain "A" in Fig. 1a). This is the ARM standard analysis domain that was used to produce the forcing data for earlier ARM field campaigns at SGP. To examine how the analyzed budget structure changes with the analysis domain size, we also perform additional analyses over two smaller domains (Domains "B" and "C" in Fig. 1a), which represent an area with diameters of approximately 150 km and 75 km, respectively. The large-scale forcing derived over these domains with different sizes could be used for modeling various-scale convective systems. Locations of the sounding stations and the analysis grid points are shown in Fig. 1a. It is seen that the location of these sounding stations either overlaps with the analysis grid or is close to it. In the following discussion, the analysis domain refers to the standard domain "A" unless the two smaller domains are explicitly indicated. The temporal and vertical resolutions used in all analyses are 3 hours and 25 hPa, respectively.

All sounding sites used Vaisala model RS92-SGP radiosondes. Humidity measurements from these radiosondes include several well-documented errors including bias (systematic) errors, random errors and sensor time-lag errors [e.g. Milosevich et al., 2009]. We have applied the empirical mean bias correction derived by Milosevich et al. [2009] through an intercomparison study with a cryogenic frost-point hygrometer. After applying these corrections a comparison with independent observations of the precipitable water vapor from a microwave radiometer at the ARM SGP CF showed reasonable agreement and gave confidence that the corrections were correct. More details regarding the MC3E sounding operations, data processing and analysis can be found in *Jensen et al*. (unpublished paper, Jensen, M. P., T. Toto, D. Troyan, P. Ciesielski, D. Holdridge, J, Kyrouac and J. Schatz et al.,

Accepted Article

The MC3E Sounding Network: Operations, Processing and Analysis. Submitted to Atmos. Meas. Tech., 2014).

The dry bias corrected radiosondes described in Jensen et al [2014] are used in the analysis. The objective analyses of the sounding measurements of temperature, wind and humidity at the analysis grid points are done with the background fields from the National Oceanic and Atmospheric Administration (NOAA) rapid update cycle (RUC) analyses using the Cressman scheme [Cressman, 1959]. The *Cressman* scheme uses a weighting function that depends on the distance between an observation station and an analysis grid point, as well as the difference between observations and the background. The interpolation is carried out for the difference field between observations and the background. If there is no measurement within a specified distance of an analysis grid point, the scheme will only take the background field as the analysis.

The required surface and TOA constraints for the variational analysis are obtained from the ARM SGP extensive surface observation network and the Geostationary Operational Environment Satellite (GOES) narrowband brightness temperature, respectively. Table 1 lists these required constraint variables and their data sources. Locations of these surface instruments are shown in Fig. 1b. Sampling of surface measurements in calculating area-averaged quantities is a potential concern for variables that have large spatial variabilities. To reduce sampling biases, we lay the 0.5^0 x 0.5^0 GOES grids over the analysis domains and then derive the surface quantities in each small grid box. If there are actual measurements within a 0.5^0 x 0.5^0 grid box, simple arithmetic averaging is used to obtain the subgrid means. If there is no actual measurement in a 0.5^0 x 0.5^0 box, then a Barnes scheme [Barnes, 1964] is used to fill the missing data. Domain averages of these quantities are obtained by using values from the 0.5^0 x 0.5^0 grid boxes within the respective analysis domains. More details of

Accepted Article

the variational analysis method and its implementation to ARM data can be found in Zhang et al. [2001].

Earlier studies [Zhang et al., 2001; Xie et al., 2004] have shown that surface precipitation is the most dominant constraint for the variational analysis during precipitation periods. To investigate the impact of uncertainties in the surface precipitation on the derived budget terms, an ensemble analysis, which contains 13 ensemble members, was carried out using the constrained variational objective analysis approach. The uncertainty range in precipitation is derived based on differences in two independently developed precipitation datasets: the Arkansas River Basin Forecast Center (ABRFC) precipitation [e.g., Young et al., 2000] products and the bias-corrected National Severe Storm Laboratory (NSSL) National Mosaic and Multisensor Quantitative Precipitation Estimate (QPE) (NMQ) Next-Generation Radar (NEXRAD)-based precipitation [e.g., Zhang et al., 2005] products (Table 1). The uncertainty range also takes into account that the fractional root-mean-square error (RMSE) of areal estimates of rain is often found to exceed 40% (relative to mean rain rate) in conventional radar-based rainfall algorithms [e.g., Ryzhkov et al., 2005; Giangrande et al., 2014]. We assume maximum spatial and temporal correlation of precipitation rate uncertainties across the analysis domain. The upper and lower bounds of the precipitation uncertainty range are listed in Table 2. The first 11 ensemble members of precipitation rates are calculated by

$$P_i = P_L + (P_U - P_L) \times i \times 0.1 \quad (1)$$

where i = 0 to 10. Two additional ensemble members are the precipitation rates obtained from ABRFC product and NSSL NMQ product, respectively. Note that the ensemble analysis is only performed over Domain “A”.

Accepted Article

3. Overview of the observed convective systems and their environments

The Hovmoller diagram of hourly NMQ NEXRAD precipitation (Fig. 2) depicts the time evolution and east-west propagation of the convective systems that passed over the ARM SGP site. Note that the west-east boundary of the sounding array is bounded by the two solid white lines in the figure. Late April and into early May during MC3E featured discrete convective storms, most often characterized as elevated nocturnal events having associated widespread stratiform precipitation. After an extended dry period, the events during the middle to late May were well-organized convection (squall line) and severe supercell thunderstorm events typically initiating to the west of the main ARM site and propagating over the site.

The earliest storms developed across northern parts of Oklahoma and along an elevated front, aided by mid to upper-level ascent associated with the passage of an upper level trough. These nighttime elevated convective cells were relatively shallow in depth, removed from the surface boundary forcing features located in southern Oklahoma also responsible for ongoing convection. Corresponding radiosondes showed a very dry and stable boundary layer, as well as elevated instability in mid-levels above 600 hPa. In contrast, the organized convective events from mid-late May were mostly associated with substantial larger-scale forcing including the passage of strong surface features (cold front, dry line), as well as additional afternoon cell triggering supported by the passage of shortwave troughs. For simplicity, we use the labels “Elevated Convection” to refer to the late April and early May discrete nocturnal elevated convective episodes and “Organized Convection” to refer to the middle to late May squall line and severe supercell thunderstorm events in discussions that follow.

The above discussion indicates that the convective events observed during MC3E were often associated with meso-scale propagating convective systems which may not be well

Accepted Article

captured by the current sounding array with a size of around 300km by 300km. However, by examining the NMQ-NEXRAD precipitation data over the region (not shown), we found that almost all of individual convective cells related to the convective events considered for this study initiated well within (April 23-24, May 1, 11, 24, 25) and/or typically towards the western edge of the sounding array (April 25, 27, May 20). These systems then continued to grow and enhance within the sounding array forced by the large-scale disturbance in the domain. Figs. 3 and 4 show snapshots for four selected "Elevated Convection" and four "Organized Convection", respectively, during their mature stages based on NMQ-NEXRAD instantaneous radar precipitation rates. These selected convective events will be discussed in more detail in the following sections. These figures clearly show that a large portion of each storm was located within the sounding array, which indicates that the large-scale structures and diabatic heating and moistening and their interactions could be reasonably captured by the sounding array. It is seen that the squall line (May 11 and 20) and deeper supercell (May 24 and 25) convective episodes exhibit a much higher intensity than the early season elevated convective storms.

The large-scale circulation during MC3E was characterized by strong westerlies in the mid- to upper troposphere where a southerly wind and a northerly wind generally alternated between wet and dry periods (Figs. 5a, b, d). In the lower troposphere, northeasterlies prevailed during the periods when the elevated storms happened while southeasterelies dominated the squall line and deeper convective periods. The southeast winds brought in a sufficient warm moist air to the experiment region from the Gulf of Mexico to support the squall line systems (not shown). As shown in Figs. 5c-d, the low-level atmosphere (below 715 hPa) was warmer and wetter for squall lines compared to the earlier scattered elevated storms. The low-level warming and moistening provided a favorable large-scale condition to initiate and maintain these intense convective events.

Accepted Article

Figure 6 shows the time series of domain mean precipitation rates from ABRFC product and the convective available potential energy (CAPE) and convection inhibition (CIN) calculated from the domain-averaged soundings and CF soundings, respectively. CAPE is calculated under the assumption that an air parcel ascends along a reversible moist adiabat with the originating level at the surface. CIN is the negative value of CAPE between the level of free convection and the surface. For the CAPE/CIN at the CF ARM radiosonde observations are used.

The late April and early May elevated convective storms occurred in a rather stable environment, in which CAPE was weak or no CAPE was detected particularly by the domain-mean soundings. This is largely due to the fact that these systems occurred at night (see Table 3) with a very stable boundary layer. It is also noticed that the boundary layer was very dry during these periods. As shown in Figure 7a, which displays the initial soundings at the CF for the 1 May event, the air was very dry at levels below 600 hPa while it was close to saturation at levels between 600 hPa and 500 hPa. This would suggest that convection might initiate at mid-levels for this event. In addition to synoptic forcings such as the mid to upper-level ascent associated with the passage of an upper level trough as discussed earlier, the mid-level convection might be also partially due to a destabilization process caused by the mid- and upper level clouds that were observed just before these scattered storms occurred as shown later. Presumably, the cooling at cloud top and warming at cloud base by longwave radiation destabilized the atmospheric column below a high stratiform layer and initiated convection at mid-levels. The depth of the unstable layer increased as the systems continued to evolve. This eventually led to deep convection that developed from the boundary layer. This upper-level destabilization process through cloud-radiation interactions was suggested by *Lee et al.* (2010) to be one of the major mechanisms for the formation of nocturnal deep convection at SGP through a cloud resolving modeling study. We have further examined the

Accepted Article

dynamic CAPE change rates as defined in Xie and Zhang [2000] to see if large-scale upward motion and low-level moisture convergence could act to destabilize the atmosphere. We found that there is no surface-based CAPE detected due to the large-scale forcing. This further implies that the elevated convection is likely caused by top-down destabilization through cloud-radiation interaction and/or middle-upper level disturbances.

In contrast, the mid and late May convective regimes occurred in the morning or early afternoon (Table 3). Large CAPE with strong diurnal variation was diagnosed before the thunderstorms developed. CIN is just opposite to CAPE, acting to prevent convection from consuming the CAPE immediately when it is generated. The initial soundings at the CF were much warmer and moister in the lower troposphere compared to the elevated storm soundings. An example is shown in Fig. 7b for a strong squall line that was observed on 20 May. It is seen that the soundings were near saturation at levels below 800 hPa while they were rather dry in the middle troposphere, suggesting that convection had its roots in the destabilized boundary layer.

The large diurnal variability exhibited in CAPE is due to the strong solar diurnal heating over land in warmer months. It is clear that a positive CAPE is not a sufficient condition to trigger convection. This presents a big challenge for the CAPE-based closure schemes implemented in many climate models for deep convection. Earlier studies have shown that most climate models fail to capture the nocturnal convection and produce overly active convection during the day in the warm season at SGP [Xie and Zhang, 2000].

Figure 8a shows the clouds measured by the ARM surface remote sensing instruments, including a 35 GHz Ka-band ARM Zenith-pointing Radar (KAZR), Micropulse Lidar (MPL), and laser ceilometers at the ARM SGP CF. The figure is constructed by integrating measurements from KAZR, MPL, and laser ceilometers using the ARSCL (Active Remote

Accepted Article

Sensing of CLouds) algorithm [Clothiaux et al., 2000; Kollias et al., 2007] with the method described in Xie et al. [2010b], which removes the radar echoes below the ARSCL cloud-base using the ARM laser ceilometers and micropulse lidar measurements. The observed clouds correspond well to the relative humidity (RH) field (Fig. 8b), which shows a very dry mid-troposphere during non-precipitating periods. The dry air is mainly a result from subsidence and horizontal advection that transported drier air into the experiment region, which will be discussed later.

There are distinct features in the clouds and RH between the earlier elevated convective storms and the later squall line and supercell events as shown in the composite profiles (Fig. 9). The composite analysis is conducted to better understand how large-scale flow affects atmospheric stability and interacts with convection. Since both types of convective systems observed during MC3E are primarily associated with propagating convective episodes and have a short lifetime, it is difficult to perform a typical life cycle analysis. The composite analysis is done here by classifying the progression of these systems into four stages based on the intensity of diabatic heating. Stage 1 is the time right before these convective systems initiate where the diabatic heating is usually less than 1 K/day. Stage 2 is the period when convection grows but the heating is often 40% less than at Stage 3. Stage 3 is the time when the systems are well developed within the analysis domain. This is often the time when precipitation or diabatic heating reaches their maximum values. Stage 4 is a time when the heating has decreased substantially, usually 40% less than at Stage 3. All of the eight major MC3E convective events shown in Figs. 3 and 4 are utilized to construct these composite profiles. Since the 25 April case occurred right after the 23-24 April event, no Stage 1 is identified for it. The observation times for the selected cases at each stage are listed in Table 3.

Accepted Article

Before the elevated systems developed, clouds associated with the trailing stratiform region of other convective systems that have already propagated to the east of the site were located primarily in the upper troposphere, having a general absence of clouds below 765 hPa (Fig. 9a). This is consistent with the very dry boundary layer where RH is less than 50% (Fig. 9c). The longwave cooling at cloud top and warming from below is likely one of the major mechanisms responsible for the initial destabilization of the atmospheric column at mid-levels. As these storms continued to evolve, clouds began to occur at low- and mid-levels associated with a large increase of RH there. The increase RH is mostly due to positive advection of moisture (probably along with cloud) into the array as shown later. The top-down destabilization process was discussed extensively in Lee et al. [2010] and was also found in other modeling and observational studies [e.g., Webster and Stephens, 1980; Randall et al., 1991]. Despite the weak peak seen around 265 hPa, the majority of clouds were still located at middle and low levels at Stages 3 and 4 when the storms were at their maximum intensity or late development stage.

Compared to the elevated storms, the organized convective events occurred in an environment with a very moist boundary layer and a plenty of low clouds (Figs 9b and 9d). However, the middle and upper troposphere were very dry and had few clouds during Stage 1. This is different from tropical systems that often show a significant amount of middle level clouds acting to moisten mid-troposphere preceding the major convective systems [Johnson et al., 1999]. The lack of congestus stage may be partially due to the combination of small number of cases and a vertical point measurement, which may miss the developing stage of the storm. However, as discussed later radiosonde data indicate a divergence layer between 665 hPa and 365 hPa, consistent with the lack of mid-level clouds. This suggests that more cases and scanning cloud radars are needed to fully characterize various stages of the convections. In contrast again with the nocturnal elevated storms, the mid- and particularly

Accepted Article

high clouds developed rapidly as the systems continued to evolve. The peak was seen around 265 hPa when the systems were at their maximum intensity, suggesting the formation of deep convection with large anvils in these intense squall lines at this stage.

Corresponding to these convective activities, the analyzed large-scale circulation featured low-level convergence and upward motion. The maximum ascending motions were seen in the middle and upper troposphere (Figs. 10). Strong low and mid-level divergence and downward motion dominated the dry periods. The composite profiles (Fig. 11) clearly demonstrate the structure difference in the large-scale dynamic fields between the elevated weaker storms and the squall line and supercell cases. For example, the considerable low-level convergence shown in the deeper convective atmosphere (Fig. 11b) at Stage 1 is not seen in the elevated discrete storms (Fig. 11a). The mean divergence profile in the squall lines shows divergence between 665 hPa and 365 hPa, consistent with the general lack of clouds at these levels. At Stage 3 when convection reaches its maximum intensity, all convective events exhibit strong convergences that extend from the surface to the middle troposphere. The non-divergence level is higher in the squall lines than the elevated storm cases, which leads to a much stronger and deeper ascending motion diagnosed from the squall line soundings (Figs. 11c and 11d). The divergence behaviors were consistent with those found in Hopper and Schumacher [2009, 2012], which systematically examined variations in divergence profiles associated with environmental and storm type differences (including elevated convection and organized convection) in midlatitude convective systems observed in Southeastern Texas. The level of the largest upward motion is located at around 515 hPa in the elevated storms, while it is around 365 hPa in the squall lines and deeper convective cases. These mature stage behaviors were consistent with observed profiles of the vertical velocity available from ARM 915 MHz profilers during MC3E campaign events [e.g., Giangrande et al., 2013]. The vertical structure of upward motion in the squall lines and

Accepted Article

deeper convective cases is also similar to that shown in Gallus and Johnson [1991] that studied an intense midlatitude squall line case observed during the OK PRE-STORM (Oklahoma-Kansas Preliminary Regional Experiment for STORM-Central) project, but the level of maximum upward motion is slightly lower (400 hPa) in Gallus and Johnson [1991] At Stage 4, the later May events show a double-peak structure in the upward motion with the primary peak located around 365 hPa and the secondary, much weaker one at 865 hPa, associated with stratiform clouds and shallow convection. This feature is not clearly seen in the earlier MC3E storms.

It should be noted that the ARM cloud information is not assimilated into the variational analysis. The consistency between clouds and the analyzed large-scale structures provides an additional check on the quality of the heat and moisture budgets diagnosed from the variational analysis. These results suggest that the variational analysis has produced a reasonable dynamic structure of these cloud systems based on the MC3E soundings, which gives us confidence in the following budget analysis.

4. Heat and moisture budgets

As defined in Yanai et al. [1973], the heat ($Q1$) and moisture budget ($Q2$) equations can be written as:

$$Q_1 = \frac{\partial s}{\partial t} + \vec{V}_h \cdot \nabla s + \omega \frac{\partial s}{\partial p} \tag{2}$$

$$Q2 = -L\left(\frac{\partial q}{\partial t} + \vec{V}_h \cdot \nabla_p q + \omega \frac{\partial q}{\partial p}\right) \tag{3}$$

Accepted Article

where s is the dry static energy, q the water vapor mixing ratio, $\vec{V}_h$ the horizontal wind vector, ω the vertical velocity in pressure coordinates, and L the latent heat of vaporization. As discussed earlier, the terms $Q1$ and $Q2$ are the residuals of heat and moisture budgets and include the collective effects of subgrid-scale processes, such as radiation, convection, and turbulence. In a highly convective situation, heating and drying from convection may have the most significant contributions to $Q1$ and $Q2$.

4.1. Heat budget

Figure 12 displays the heat budget terms over the analysis domain. The strong diurnal heating near the surface in both the heat storage term ($\frac{\partial s}{\partial t}$, Fig. 12a) and $Q1$ (Fig. 12b) is due to the strong solar heating and sensible heat flux over land during the day. The fluctuation of $Q1$ corresponds well with the surface precipitation. Over these periods, a strong heating associated with the latent heat release is diagnosed in the mid- and upper troposphere. A cooling is seen in the lower levels, presumably related to the evaporation of precipitation. For most of the experiment period, the horizontal advection of heat ($-\vec{V}_h \cdot \nabla s$, Fig. 12c) tends to warm the lower and mid-troposphere below 515 hPa and the levels above 265 hPa, and somewhat cool the levels in between. The vertical advection ($-\omega \frac{\partial s}{\partial p}$, Fig. 12d) shows a strong mid- and upper level cooling over precipitation periods and a strong warming during dry periods. This cooling/warming is primarily associated with the large-scale upward/downward motions as shown in Fig. 10b.

More detailed composite analyses of these budget terms are shown in Figs. 13 and 14 for the earlier elevated storms and the deeper later events, respectively. For the elevated earlier storms, both $Q1$ and the vertical transport of heat (Figs. 13b and 13d) are weak due to the

Accepted Article

lack of convective activities and upward motions at Stage 1. The horizontal advection of heat (Fig. 13c) is the major contributor to the cooling seen near the surface in the storage term (Fig. 13a). As the earlier elevated systems start to grow and reach their maturity, the $Q1$ profile shows large heating in the middle troposphere and a considerable cooling below, especially at Stages 2 and 3. This structure was also found in earlier studies for mid-latitude storms [e.g., Kuo and Anthes, 1984]. In tropical convective systems, the heating usually extends through the entire troposphere [e.g., Xie et al., 2010a]. The heating in $Q1$ at these stages is primarily balanced by the cooling associated with upward motion. The lower-level cooling is mainly due to the evaporation of precipitation and clouds.

$Q1$ is much stronger and extends much higher in the squall line and supercells when the system reaches its maximum intensity (Fig. 14b). Note that the scale in x-axis used in Figs 14b and 14d is two times larger than that in Figs. 13b and 13d. The maximum in upper-level heating occurs at around 340 hPa for these later May events compared to 515 hPa in the earlier weaker elevated storms when both types of systems reach their maximum intensity. Similar to the elevated events, a notable cooling is also seen in the lower troposphere at Stages 3 and 4. The strong heating in $Q1$ is primarily balanced by the cooling from the vertical transport of heat (Fig. 14d), leading to a relatively small change in the storage term (Fig. 14a). The horizontal advection (Fig. 14c) is large in the upper troposphere above 365 hPa and is also important in the lower troposphere. It is worth noting that a cold horizontal advection is seen near the surface before the elevated storms develop, while a near surface warm horizontal advection is found before the deeper and squall line systems develop. This reflects the difference in the near surface flow between these two types of convective systems as we discussed earlier. The warming below 815 hPa at Stage 1 in Fig. 14b is due to the solar radiation and sensible turbulent flux during the day.

Accepted Article

The diagnosed Q1 profile in the deeper events is similar to that in Kuo and Anthes [1984] and Gallus and Johnson [1991], which also indicated an upper level heating between 400 hPa and350 hPa. However, the level of maximum upward motion in Kuo and Anthes [1984] is located around 550 hPa, much lower than what found in Gallus and Johnson [1991] and the current study. The difference could be partially from the larger domain [550 km x 550 km] used in Kuo and Anthes [1984] compared to the 300 km x 300 km domain used in this study. Sensitivity of the analyzed budgets to the analysis domain size will be discussed in Section 5. The difference may also suggest variations among different convective systems and the need for more case studies.

4.2. Moisture budget

The time-pressure cross sections of individual terms in the moisture budget are displayed in Figure 15. In general, the horizontal advection of moisture ($-\vec{V}_h \cdot \nabla_p q$, Fig. 15c) plays an important role in moistening the lower troposphere while the vertical advection ($-\omega \frac{\partial q}{\partial p}$, Fig. 15d) is the key process that transports moisture to the mid- and upper troposphere for convection to consume. The $Q2$ profile (Fig. 15b), which is normalized by L, indicates that the drying associated with convection can reach up to 265 hPa in the strong convective events, although the majority of the drying occurs at lower levels. As a result, the storage term ($\frac{\partial q}{\partial t}$, Fig. 15a) generally shows a moistening when the systems are at their early development stages (Stages 1 and 2), and a drying when the systems are well developed or begin to dissipate (Stages 3 and 4), which can be seen clearly in the composite analysis figures (Figs. 16 and 17).

For the earlier elevated storms, the storage term shows a weak moistening below 765 hPa (Fig. 16a) before the systems develop. This is largely due to the evaporation of clouds and the

Accepted Article

vertical transport of turbulence fluxes as shown in $Q2$ (Fig. 16b). The mid- and low level moistening from the horizontal advection (Fig. 16c) also contributes to this moistening. At this stage, the vertical advection is weak (Fig. 16d). As the systems evolve to Stages 3 and 4, a strong diabatic drying is seen at levels above 865 hPa and a considerable moistening is found below. The mid- and upper level diabatic drying is largely offset by the vertical transport of moisture. It is noted that there is a lack of moisture supply from advection near the surface for these storms.

In contrast, there is persistent moisture supply from the horizontal advection near the surface for the later May events (Fig. 17c). The low-level moisture supply is from the near surface southeasterlies, which brings warm-moist air into the region. The region of the moist convergence extends up to 565 hPa as the systems grow to Stage 2, which contributes significantly to the moistening at levels above 815 hPa shown in the storage term (Fig. 17a). The storage term shows a strong drying at levels below 665 hPa as the systems reach their maxima, primarily due to convection (Fig. 17b). The mid- and upper moisture supply for convection is purely due to the vertical moisture transport at this stage (Fig. 17d). It is noted that the primary peak in $Q2$ is located in the lower troposphere along with two weaker peaks located at 715 hPa and 490 hPa, respectively. In addition to the convective drying due to shallow clouds, the vertical turbulent fluxes should also contribute significantly to the low-level drying in $Q2$. At Stage 4, $Q2$ shows a strong drying at low levels associated with the development of boundary layer clouds and a weak moistening at mid-levels due to the evaporation of precipitation. The large drying seen in the storage term at this stage is mainly due to the dry advection of moisture from the horizontal.

The above discussion indicates the important role of the moisture transport in the development of mid-latitude convective systems. This is further illustrated in Fig. 18, which examines the correlation among the rainfall rates, column-integrated moisture convergence,

Accepted Article

and moisture storage term for those precipitation events that occurred in April and May. For most of the precipitation events (except for 24 April and 20 May], there is clear evidence that the moisture convergence was leading the convection, acting to moisten the pre-environment for these convective systems. During this period, the moisture storage term showed a considerable increase. It dropped rapidly around the time when the systems reached their maxima. At this stage, consumption of water vapor by convection (indicated by precipitation] exceeds the large-scale moisture supply, leading to a large decrease of moisture in the integrated storage term.

5. Sensitivity to precipitation uncertainty and domain size

5.1. Variation of budget structure with precipitation uncertainty

An ensemble run with thirteen ensemble members was performed with the variational analysis over the standard analysis domain "A" to examine the impact of uncertainties in the surface precipitation on the derived budget structures. The range of uncertainty in the surface precipitation is determined by the difference between the ABRFC product estimate and the NSSL NMQ dataset, as well as considering an approximate 40% fractional RMSE for areal estimates of rain associated with radar-based rainfall products. Figure 19a shows the ensemble precipitation rates for the period between 00Z 19 May and 00Z 26 May for demonstration purposes. Similar results are seen for other periods. It is seen that the domain-averaged rainfall rates derived from ABRFC product are very similar to those obtained from the gauge-corrected NMQ product for the 20 May event. Both are close to 50% of the uncertainty range between the upper and lower bound of the estimated precipitation. However, although both products utilize gauge and NOAA WSR-88D NEXRAD radar systems to help produce these estimates, the rainfall rates are significantly larger from the

Accepted Article

NMQ product for the isolated supercell events that occur on the later campaign days (23, 24 May and 25 May). This spread is to be expected based on the details of how each product handles isolated convective events possibly containing hail and the associated precipitation estimates therein.

Figures 19b and 19c display the variation in the vertical profile of the vertical velocity and Q1 averaged over the period between 09Z 20 May and 15Z 20 May when a strong squall line resided over the experiment domain. It is seen that the strength of vertical motion and diabatic heating is just proportional to the precipitation rates used in the analysis. Larger precipitation rates lead to stronger ascending motion and greater diabatic heating. Generally, the precipitation uncertainty does not affect the level of maximum heating and the general structure of $Q1$. It is worth noting that the uncertainty in precipitation could change the sign of the large-scale forcing and diabatic heating when they are weak. For example, the vertical velocity can change from a moderate upward motion to a weak downward motion at levels below 715 hPa with the decrease of precipitation rates for the 20 May case. Similar feature is also seen in $Q1$.

5.2. Variation of budget structure with domain size

To examine how the heat and moisture budgets change with the size of analysis domain, additional analyses were performed over two smaller domains, i.e., Doman "B" and Domain "C" as shown in Fig. 1a. The observed surface and TOA fluxes averaged over the respective domains are used as the constraints in the variational analysis. Therefore, the variations of budget structure shown below are due to changes not only in domain size, but also in these surface constraints. This should be bore in mind in the discussion below. It should be also noted that the analysis over Domain C is largely dependent on the background fields from RUC analyses since its analysis grids are far distant from the boundary sounding stations. By

Accepted Article

adjusting the atmospheric state variables from RUC analyses to balance the observed column budgets of mass, heat, and moisture, *Xie at al*. [2004) showed that the quality of the derived budget terms could be significantly improved.

Figure 20a compares the mean precipitation rates over Domains "A", "B", and "C" for the same period as that shown in Fig. 19a. Differences are seen in the intensity and timing of these precipitation events as the analysis domain size changes, reflecting the large spatial variability in precipitation.

Figures 20b and 20c respectively display the variation in the vertical structure of the vertical motion and $Q1$ averaged over the same period as that in Figs. 19b and 19c. Similarly, larger precipitation rates correspond to stronger upward motion and greater diabatic heating. The vertical structure of the vertical velocity and $Q1$ is similar over the three analysis domains except for the level of maximum upward motion over the smallest domain, which is slightly lower than that over the bigger domains. This may be because a few stratiform clouds contained in the smallest domain as indicated by Fig. 20c, in which the secondary peak around 340 hPa in $Q1$ over Domain "C" is not as clear as that shown over the two bigger domains.

6. Summary and discussion

We have performed a budget analysis to understand interactions between cumulus convection and its environment in the midlatitudes with data collected from the recent field MC3E campaign that was conducted from 22 April – 6 June 2011 at the ARM SGP site. Our analysis has been focused on the variations of the structures in elevated thunderstorms and deeper convective events, two bulk types of convective systems that are often observed in the late Spring and early Summer in this region. A constrained objective variational analysis approach, which uses surface and TOA flux observations as the constraints, was used to

Accepted Article

derive the large-scale state structures and $Q1$ and $Q2$ profiles from the MC3E sounding array. The analyzed fields correspond well with the ARM radar measurements of cloud frequency of occurence, which were not assimilated into the analysis. This provides an independent check on the diagnosed heat and moisture budgets.

Distinct large-scale structures and diabatic heating and drying profiles were found with the two types of convective systems. The examined elevated events were nocturnal precipitation cases. These events initiated in an environment with little CAPE identified from the soundings and were consistent with a very dry boundary layer. Convection in these systems is thought to be initiated at mid-levels partially as a result of cloud-radiation interactions in additional to synoptic forcings. Long-wave cooling at the top of high stratiform clouds and warming below destabilized the atmospheric column at mid-levels. Deep convection eventually occurred from the boundary layer as the systems evolved with time. This top-down destabilization process for nocturnal convection at SGP has been tested in *Lee et al.* [2010] through a cloud resolving modeling study. The current analysis has provided observational evidence that supports such a hypothesis.

In contrast, the later May supercell and squall lines developed in the morning or early afternoon. Their pre-environments were associated with a large amount of CAPE along with a near saturated boundary layer. The latter was largely due to the persistent near surface southeasterlies that brought in sufficient warm and moist air return to the experiment region from the Gulf of Mexico. Very strong deep convection occurred rapidly with its roots in the boundary layer.

As the convective systems reached their maturity, the diabatic heating mainly from latent heat release was much stronger and extended much higher in the squall line type events than in the elevated systems. The level of maximum heating was located at around 340 hPa in the

Accepted Article

organized deep convection, while it was around 515 hPa in the elevated storms. Accordingly, the upward motion in the squall line type events was much stronger and reached much higher altitudes than that in the earlier MC3E events. For example, the primary peak of the upward motion was located at around 365 hPa in later May events as compared to 515 hPa in the earlier April and May events. It is worth noting that the $Q1$ profile in both types of convection exhibited a considerable cooling in the lower troposphere, which is not often seen in convective systems over tropical oceans. This unique feature in $Q1$ associated with mid-latitude convective systems has been also found in previous budget studies in this region. It is presumably due to the evaporation of precipitation and low-level clouds.

The diabatic drying in the elevated convective storms was primarily located in the middle troposphere. Below 865 hPa, a considerable moistening was found. This further suggests the existence of the evaporation of precipitation and clouds at low levels. In contrast, the diabatic drying in the deeper convective cells was located mainly in the lower troposphere, reflecting activities of low-level clouds and strong turbulent flux exchanges in the boundary layer during the day. The vertical variations of $Q2$ resembled the vertical advection of moisture in the mid- and upper troposphere where the vertical transport of moisture provided the necessary moisture supply for convection to consume.

Unlike tropical convection, where the horizontal advection of temperature can be neglected, it played an important role in the heat budget of the midlatitude convective systems. The magnitude of the horizontal temperature advection was comparable to that of the diabatic heating and the vertical transport of temperature in both the lower and upper troposphere for these selected convective systems. The horizontal moisture advection played a dominant role in moistening the lower atmosphere, particularly for the squall lines where the southeasterlies provided persistent low-level moisture supply from the Gulf of Mexico to support convection. It has been found that the column-integrated moisture convergence was

Accepted Article

leading convection in all the selected events, suggesting that the accumulation of moisture provided a favorable condition to initiate these midlatitude convective systems.

Sensitivity tests further indicated that the uncertainty in the surface precipitation mainly affected the magnitude of these analyzed fields rather than the vertical structure. The same is true with the change of the analysis domain size. However, the analysis domain size change might affect the timing and the level of maximum ascending motion and diabatic heating, depending on how these convective systems were captured by the analysis domains.

Different from earlier budget studies, which were often based on a single case [e.g. Kuo and Anthers 1984 and Gallus and Johnson 1991], the current analysis has performed a composite analysis based on multiple cases. These examined convective events were further separated into groupings of elevated thunderstorms and supercell and squall line events to examine similarities and differences between these two typical convective systems that often occur at SGP. The constrained variational analysis method used in the study has improved the quality of the analyzed large-scale structures and diabatic heating and drying profiles by enforcing the column integral of the analyzed mass, heat, and moisture to be balanced with the surface and TOA observations. Nevertheless, the number of cases studied in the current study is still far too limited. Given the large variations in the analyzed structures among different convective systems, more cases need to be analyzed in order to make the results statistically robust. The DOE ARM program has conducted more than twenty sounding Intensive Operational Periods (IOPs) at SGP over different seasons in the past twenty years. This allows us to perform a statistical study of various midlatitude convective systems over different seasons. This will be our future work.

Convective events that occur at SGP are often associated with west-east propagating meso-scale convective systems. This poses a challenge in studying the relationship between

Accepted Article

the environment observed in the sounding array and the convection because the size of current ARM sounding array may not be able to appropriately capture the environment for the entire lifecycle of these propagating meso-scale convective systems. Increase of the size of sounding array to cover bigger area to the west of the ARM SGP site should be considered in future planned major field campaigns.

It is noted that the nocturnal elevated convection over the central United States has gained increased scientific attention in recent years [Horgan et al. 2007; Corfidi et al. 2008, Lee et al. 2010]. Several field campaigns have been targeted to understand what allows convection to initiate in the presence of a stable nocturnal boundary layer, such as the International H2O Project (IHOP) (Weckwerth et al. 2004) that was conducted in 2002 at SGP to improve the understanding and prediction of convective initiation. A recently proposed multi-agency field campaign PECAN (Plains Elevated Convection At Night) (http://asr.science.energy.gov/meetings/stm/2013/presentations/PECAN-update.pdf) is specifically aimed to the nocturnal elevated convection and stable boundary layers. The current study represents one of the efforts toward understanding the mechanisms behind these commonly observed convective systems at SGP and provides useful information to the being planned PECAN field campaign.

Acknowledgments. The authors would like to thank the anonymous referees for their valuable comments that helped to clarify and improve the paper. We thank Paul Ciesielski and Richard Johnson for helpful discussion on the use of sounding data. The observational data were obtained from the ARM program sponsored by the U. S. Department of Energy, Office of Science, Office of Biological and Environmental Research, Environmental Sciences Division. Work at LLNL was supported by the DOE ARM program and performed under the auspices of the U. S. Department of Energy by Lawrence Livermore National Laboratory under contract No. DE-AC52-07NA27344. Work at Stony Brook University was supported

Accepted Article

by the DOE ASR program. Contributions from Brookhaven National Laboratory were supported by the DOE Atmospheric Systems Research under contract No. DE-AC02-98CH10886. The data can be obtained from the ARM archive (http://iop.archive.arm.gov/arm-iop/0eval-data/xie/scm-forcing/iop_at_sgp/MC3E/).

References

Barnes, S. L. (1964), A technique for maximizing details in numerical map analysis. *J. Appl. Meteorol.*, **3**, 396-409.

Clothiaux, E. E., T. P. Ackerman, G. G. Mace, K. P. Moran, R. T. Marchand, M. Miller, and B. E. Martner (2000), Objective determination of cloud heights and radar reflectivities using a combination of active remote sensors at the ARM CART sites, *J. Appl. Meteor*., ***39***, 645-665.

Cressman, G. P. (1959), An operational objective analysis scheme, *Mon. Wea. Rev., **87**,* 367-374.

Frank, W. M. (1978), The life Cycle of GATE Convective Systems. *J. Atmos. Sci.*, **35**, 1256-1264.

Frank, W. M., and J. L. McBride (1989), The vertical distribution of heating in AMEX and GATE cloud clusters. *J. Atmos. Sci.*, **46**, 3464-3478.

Gallus, W. A., and R. H. Johnson (1991), Heat and moisture budgets of an intense midlatitude squall line. J. Atmos. Sci., 48, 122–146.

Ghan S., et al. (2000), An Intercomparison of Single Column Model Simulations of Summertime Midlatitude Continental Convection. *J. Geophys. Res*., **105**, 2091-2121.

Accepted Article

Giangrande, Scott E., Scott Collis, Jerry Straka, Alain Protat, Christopher Williams, Steven Krueger (2013), A Summary of Convective-Core Vertical Velocity Properties Using ARM UHF Wind Profilers in Oklahoma. *J. Appl. Meteor. Climatol.*, **52**, 2278–2295.

Giangrande, S. E., S. Collis, A.K. Theisen, and A. Tokay (2014), Precipitation Estimation from the ARM Distributed Radar Network During the MC3E Campaign. J. Appl. Meteorol. and Climotol. *http://journals.ametsoc.org/doi/abs/10.1175/JAMC-D-13-0321.1.*

Hopper, L. J. Jr., and C. Schumacher (2009), Baroclinicity influences on storm divergence and stratiform rain: Subtropical upper-level disturbances. *Mon. Wea. Rev.,* **137**, 1338-1357.

Hopper, L. J. Jr., and C. Schumacher (2011), Modeled and observed variations in storm divergence and stratiform rain production in Southeastern Texas. *J. Atmos. Sci*., **69**, 1159–1181.

Johnson, R. H. (1984), Partitioning tropical heat and moisture budgets into cumulus and mesoscale components: Implications for cumulus parameterization. *Mon. Wea. Rev.*, **112**, 1590-1601.

Johnson, R. H., T. M. Rickenbach, S. A. Rutledge, P. E. Ciesielski, and W. H. Shubert (1999), Trimodal characteristics of tropical convection. J. Climate, 12, 2397–2418.

Johnson, R. H., and P. E. Ciesielski (2013), Structure and Properties of Madden–Julian Oscillations Deduced from DYNAMO Sounding Arrays. *J. Atmos. Sci*., **70**, 3157–3179.

Jensen et al. (2010), Midlatitude Continental Convective Clouds Experiment (MC3E), DOE/SC-ARM/10-0004.

Accepted Article

Kollias, P., E. E. Clothiaux, M. A. Miller, E. P. Luke, K. L. Johnson, K. P. Moran, K. B. Widener and B. A. Albrechet (2007), The Atmospheric Radiation Measurement Program Cloud Profiling Radars: Second-Generation Sampling Strategies, Processing, and Cloud Data Products. *Journal of Atmospheric and Oceanic Technology*, **24,** doi:10.1175/JTECH2033.1

Kuo, Y.-H., and R. A. Anthes (1984), Mesoscale budgets of heat and moisture in a convective system over the central United States. Mon. Wea. Rev., 112, 1482–1497.

Lee, M.-I., I. Choi, W. Tao, S. D. Schubert, and I.-S. Kang (2010), Mechanisms of diurnal precipitation over the US Great Plains: a cloud resolving model perspective. Clim. Dyn., 34, 419-437. Doi:10.1007/s00382-009-0531-x.

Lewis, J. M. (1975), Test of Ogura-Cho model on a prefrontal squall line case. *Mon. Wea. Rev*., **103**, 764-778.

Lin, X., and R. H. Johnson (1996a), Kinematic and thermodynamic characteristics of the flow over the Western Pacific Warm pool during TOGA COARE. *J. Atmos. Sci.*, 53, 695-715.

Lin, X., and R. H. Johnson (1996b), Heating, Moistening, and Rainfall over the Western Pacific Warm pool during TOGA COARE. *J. Atmos. Sci.*, **53**, 3367-3383.

May, P. T., J. H. Mather, G. Vaughan, C. Jakob, G. M. McFarquhar, K. N. Brown, and G. G. Mace (2008), The Tropical Warm Pool International Cloud Experiment. *Bull. Amer. Met. Soc*., **89**, 629-645.

Ninomiya, K. (1971), Dynamical analysis of outflow from tornado-producing thunderstorms as revealed by ATS III pictures. *J. Appl. Meteor*., **10**, 275-294.

Accepted Article

Randall D. A., Harsvardhan, D. A. Dazlich (1991), Diurnal variability of the hydrological cycle in a general circulation model. *J. Atmos. Sci*. **48**, 40-62.

Riehl, H., and J. S. Malkus (1958), On the heat balance in the equatorial trough zone, *Geophysica*, **6**, 503-538.

Ryzhkov, A. V., S. E. Giangrande, and T. J. Schuur (2005), Rainfall Estimation with a Polarimetric Prototype of WSR-88D. *J. Appl. Meteor.*, **44**, 502–515.

Schumacher, C., M. H. Zhang, and P. E. Ciesielski (2007), Heating structures of the TRMM field campaigns. *J. Atmos. Sci.*, **64**, 2593-2610.

Stensrud, D. J. (1996), Effects of persistent, midlatitude mesoscale regions of convection on the large-scale environment during the warm season. J. Atmos. Sci., 53, 3503-3527.

Thompson, R. M.,S. W. Payne, E. E. Recker, and R. J. Reed (1979), Structure and properties of synoptic-scale wave disturbances in the intertropical convergence zone of the eastern Atlantic, *J. Atmos. Sci*., **36**, 53-72.

Webster, P. J., and R. Lukas (1992), TOGA COARE: The Coupled Ocean—Atmosphere Response Experiment. *Bull. Amer. Meteor. Soc*., **73**, 1377–1416.

Webster P. J., and G. L. Stephens (1980), Tropical upper-tropospheric extended clouds: inferences from winter MONEX. *J. Atmos. Sci*. **37**, 1521-1541.

Weckwerth, T., D. Parsons and co-authors (2004), An overview of the International H2O Project (IHOP_2002) and some preliminary highlights. *Bull. Amer. Meteor. Soc*., **85**, 253-277.

Accepted Article

Xie, S., et al. (2002), Intercomparison and Evaluation of Cumulus Parameterization under Summertime Midlatitude Continental Conditions. *Q. J. R. Meteorol. Soc.*, **128**, 1095-1136.

Xie, S. C., R. T. Cederwall, and M. Zhang (2004), Developing long-term single-column model/cloud system-resolving model forcing data using numerical weather prediction products constrained by surface and top of the atmosphere observations, J. Geophys. Res., 109 D001104, doi:10.1029/2003JD004045.

Xie, S., and 24 co-authors (2005), Simulations of midlatitude frontal clouds by SCMs and CSRMs during the ARM March 2000 Cloud IOP. *J. Geophys. Res.*, **110**, D15S03, doi:10.1029/2004JD005119.

Xie, S., S. A. Klein, M. Zhang, J. J. Yio, R. T. Cederwall, and R. McCoy (2006), Developing large-scale forcing data for single-column model and cloud-resolving model from the Mixed-Phase Arctic Cloud Experiment, *J. Geophys. Res.*, **111**, D19104, doi:10.1029/2005JD006950.

Xie, S, T. Hume, C. Jakob, S. A. Klein, R. B. McCoy, M. Zhang (2010a), Observed Large-Scale Structures and Diabatic Heating and Drying Profiles during TWP-ICE. *J. Climate*, **23**, 57–79. doi: http://dx.doi.org/10.1175/2009JCLI3071.1.

Xie, S., and Coauthors (2010b), CLOUDS AND MORE: ARM Climate Modeling Best Estimate Data. Bull. Amer. Meteor. Soc., 91, 13–20, doi:10.1175/2009BAMS2891.1.

Xu, K.-M., R. T. Cederwall et al., and S. Xie (2002), An Intercomparison of cloud-resolving models with the ARM summer 1997 IOP data. *Q. J. R. Meteorol. Soc.*, **128**, 593-624.

Xu, K.-M., et al. (2005),.Modeling springtime shallow and deep frontal clouds with CRMs and SCMs. *J. Geophys. Res.*, **110**, D15S04, doi:10.1029/2004JD005153.

Accepted Article

Yanai, M. (1961), A detailed analysis of typhoon formation. *J. Meteor. Soc. Japan*, 39, 187-214.

Yanai, M., S. Esbensen, and J. Chu (1973), Determination of bulk properties of tropical cloud clusters from large-scale heat and moisture budgets. *J. Atmos. Sci*., **30**, 611-627.

Yanai, M., and R. Johnson, 1993), Impacts of cumulus convection on thermodynamic fields, *Meteorol. Monogr*., **46**, 39-62.

Yanai, B. Chen, and W.-W Tung (2000), The Madden-Julian oscillation observed during the TOGA COARE IOP: Global view. *J. Atmos. Sci*., **57**, 2374-2396.

Young, C. B., A. A. Bradley, W. F. Krajewski, A. Kruger, and M. L. Morrissey (2000), Evaluating NEXRAD Multisensor Precipitation Estimates for Operational Hydrologic Forecasting. *J. Hydrometeor*, **1**, 241–254. doi: http://dx.doi.org/10.1175/1525-7541(2000)001<0241:ENMPEF>2.0.CO;2

Zhang, C., J. Gottschalck, E. D. Maloney, M. W. Moncrieff, F. Vitart, D. E. Waliser, B. Wang, and M. C. Wheeler (2013), Cracking the MJO nut, *Geophys. Res. Lett*., **40**, 1223-1230. Doi:10.1002/grl.50244.

Zhang, G. J. (2002), Convective quasi-equilibrium in midlatitude continental environment and its effect on convective parameterization. *J. Geophys. Res*., **107** (D14), 4220, doi:10.1029/2001JD001005.

Zhang, J., K. Howard, and J. J. Gourley (2005), Constructing Three-Dimensional Multiple-Radar Reflectivity Mosaics: Examples of Convective Storms and Stratiform Rain Echoes. *J. Atmos. Oceanic Technol.*, **22**, 30–42. doi: http://dx.doi.org/10.1175/JTECH-1689.1

Accepted Article

Zhang, M. H., and J. L. Lin (1997), Constrained variational analysis of sounding data bases on column-integrated budgets of mass, heat, moisture, and momentum: Approach and application to ARM measurements, *J. Atmos. Sci.*, ***54***, 1503-1524.

Zhang, M. H., J. L. Lin, R. T. Cederwall, J. J. Yio, and S. C. Xie (2001), Objective analysis of ARM IOP Data: Method and sensitivity, *Mon. Weather Rev.*, ***129***, 295-311.

Accepted Article

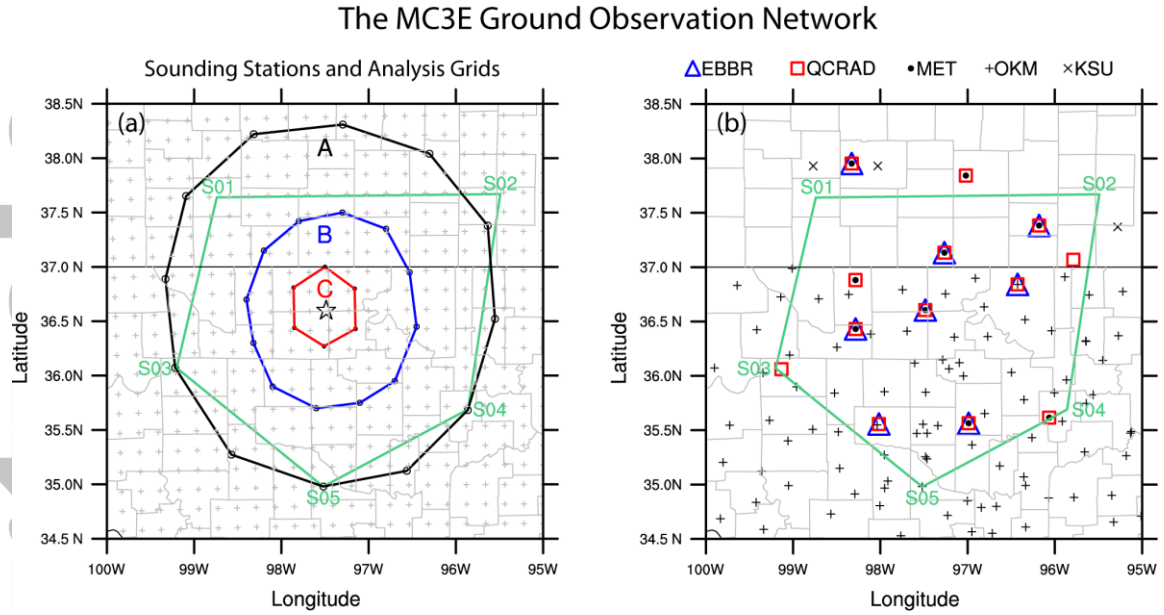

Figure 1. The ground observation network established during MC3E. a) Sounding stations (S01-S05 and central facility), variational analysis grid points (dotted), and ARM SGP CF (star). Black circle denotes variational analysis domain A with a diameter of 300 km centered at SGP CF; blue circle denotes domain B with a diameter of 150 km; red circle denotes domain C with a diameter of 75 km. b) Other surface stations available at the ARM SGP site.

Accepted

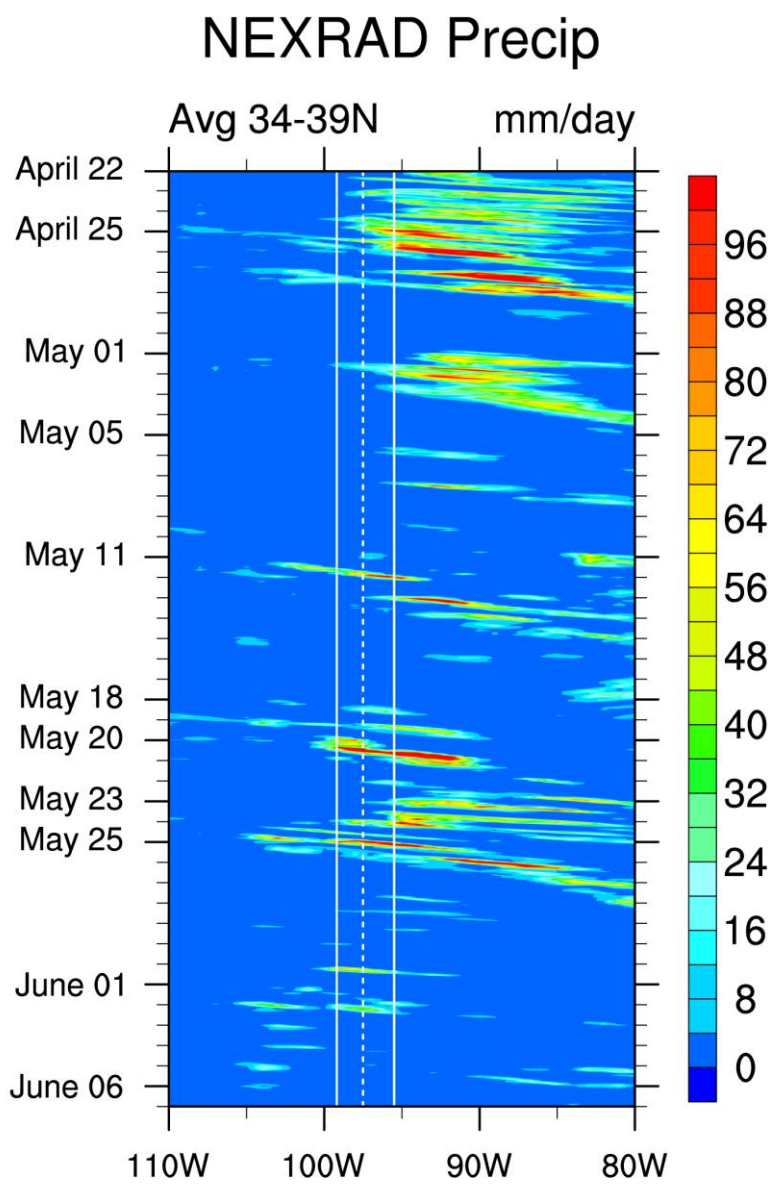

Figure 2. Hovmöller diagram of hourly bias-corrected NOAA NMQ NEXRAD precipitation averaged over 34N to 39N. The east-west boundary of the sounding array is bounded by the two solid white lines and the dashed white line indicates the location of the ARM SGP CF.

Accept

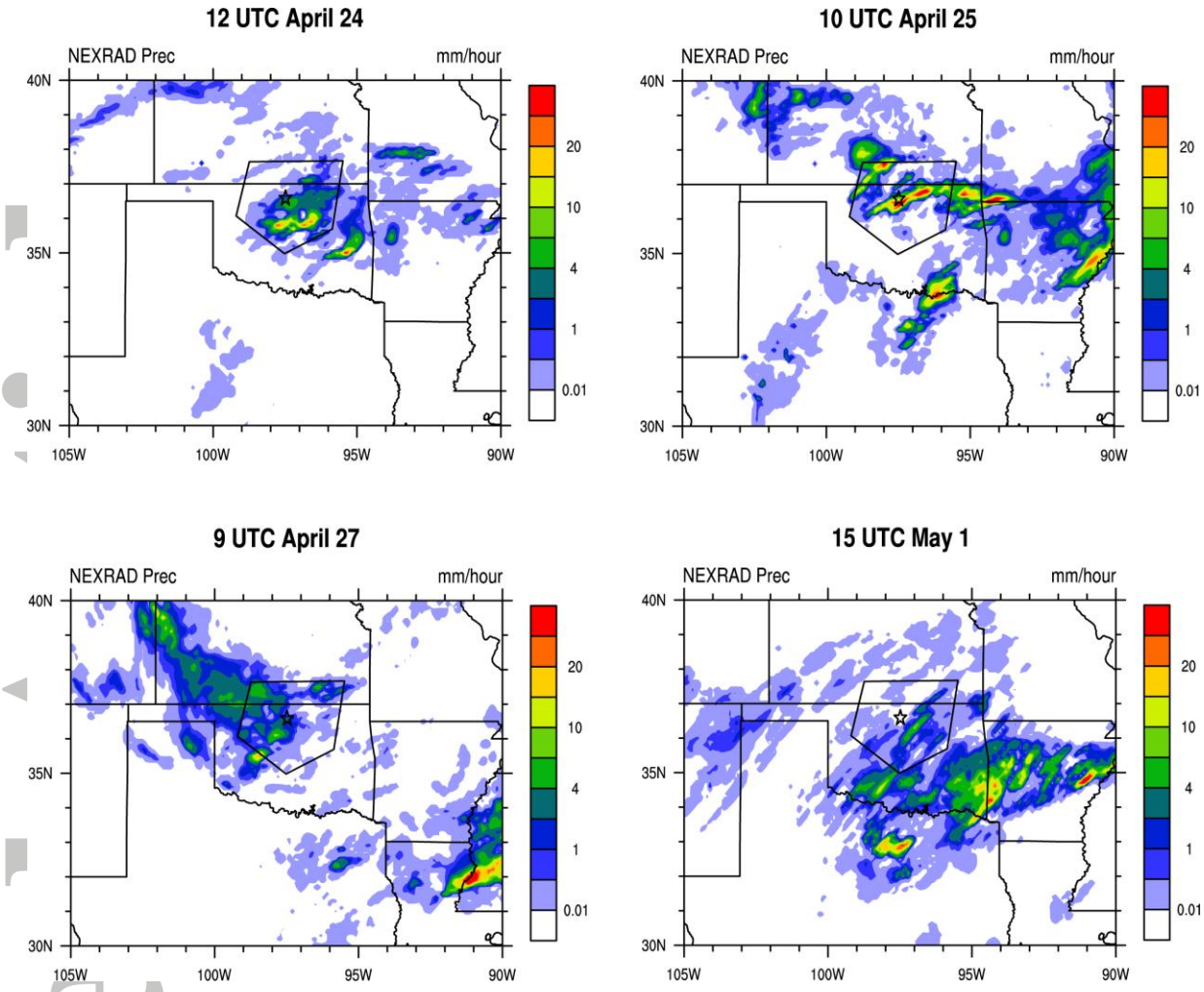

Figure 3. Images of the NOAA NMQ NEXRAD precipitation for 4 selected precipitation events associated nocturnal elevated convection. The pentagon in these figures denotes the MC3E sounding domain. Local time in SGP is 5 hours less than universal time (UTC).

Accepted

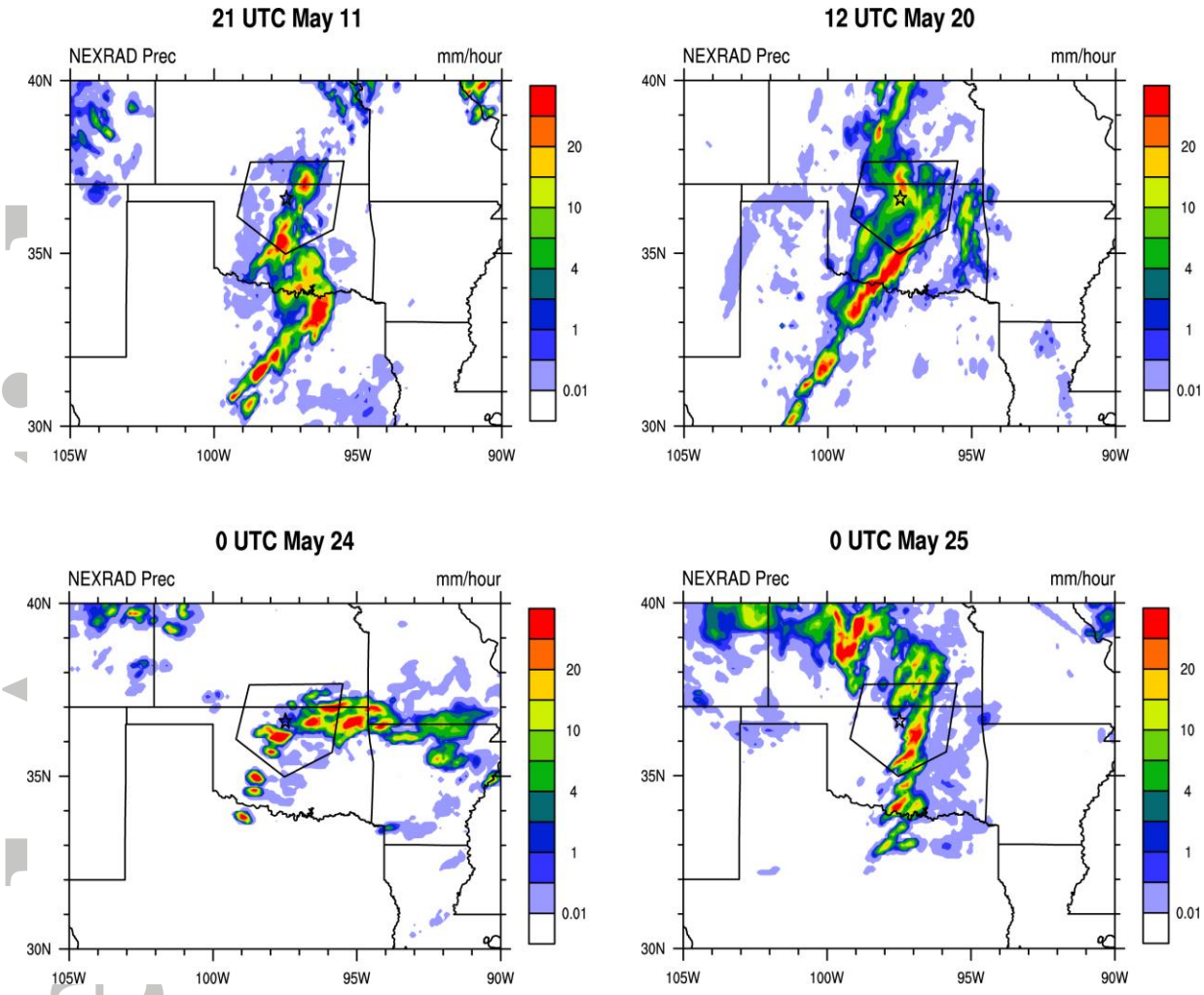

Figure 4. Images of the NOAA NMQ NEXRAD precipitation for 4 selected precipitation events associated with organized convection. The pentagon in these figures denotes the MC3E sounding domain. Local time in SGP is 5 hours less than universal time (UTC).

Accepted

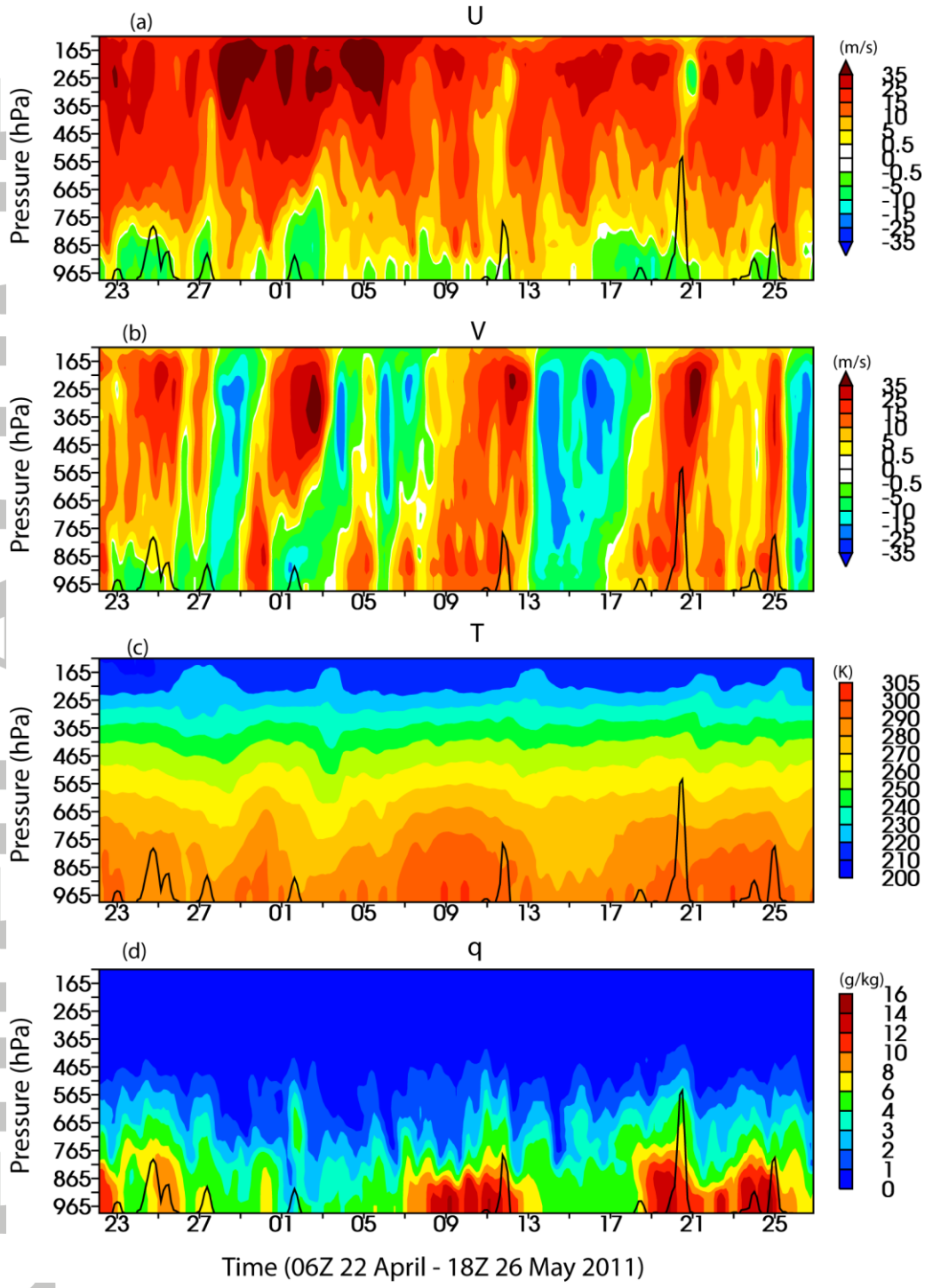

Figure 5. The time-pressure cross-sections of the analyzed (a) zonal wind (U [m s-1]), (b) meridional wind (V [m s-1]), (c) temperature (T [K]), and (d) water vapor mixing ratio (q[g kg-1]) over the analysis domain during MC3E. In these figures, black lines are surface precipitation rates. A 3-point running mean was applied to these fields for display purposes.

Accepted Article

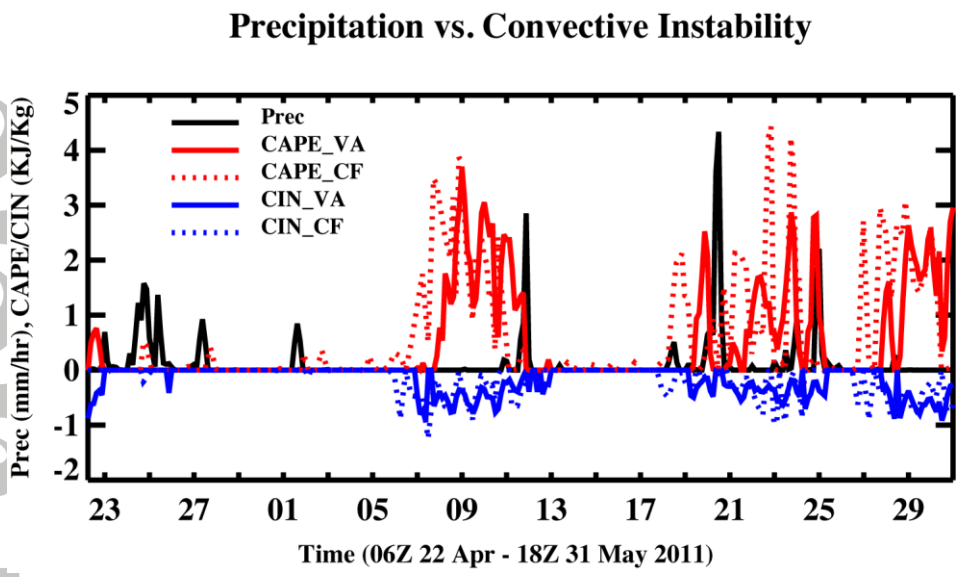

Figure 6. Observed the domain averaged ABRFC surface precipitation rates (mm hr-1) and CAPE/CIN (KJ/Kg) computed from domain-averaged soundings (CAPE-VA/CIN_VA) and CF soundings (CAPE_CF/CIN_CF).

Accepted Article

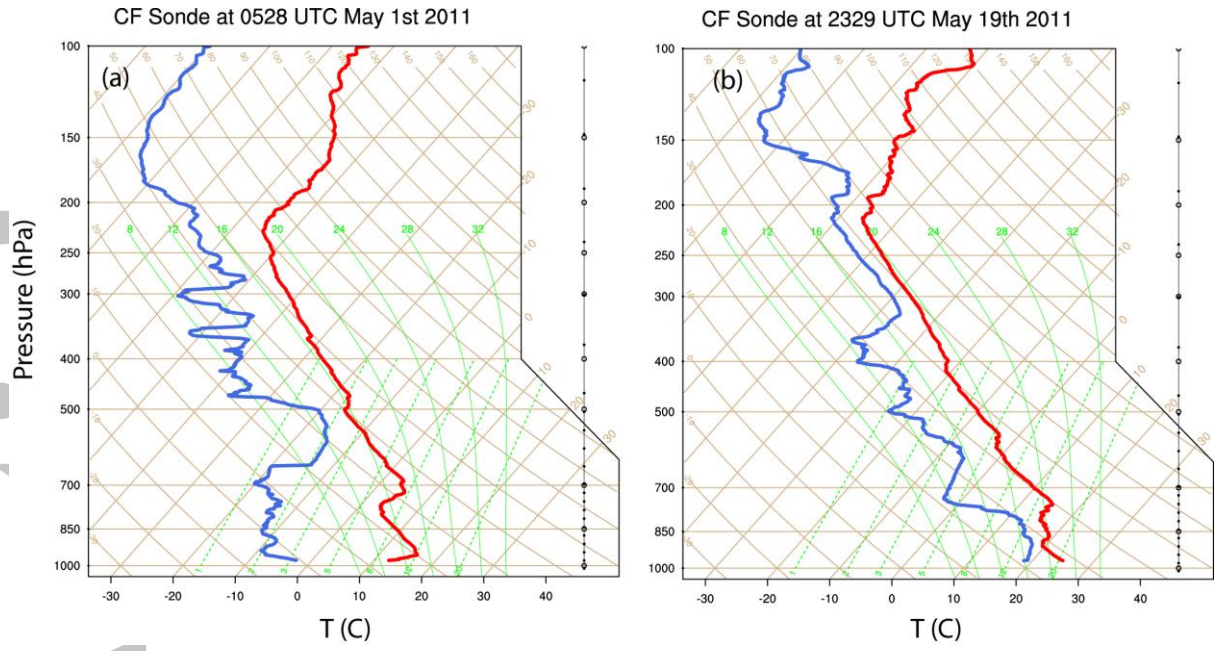

Figure 7. Temperature (T) and dewpoint soundings (Td) at the time right before convection occurred for (a) the 1 May case and (b) the 20 May case.

Accepted

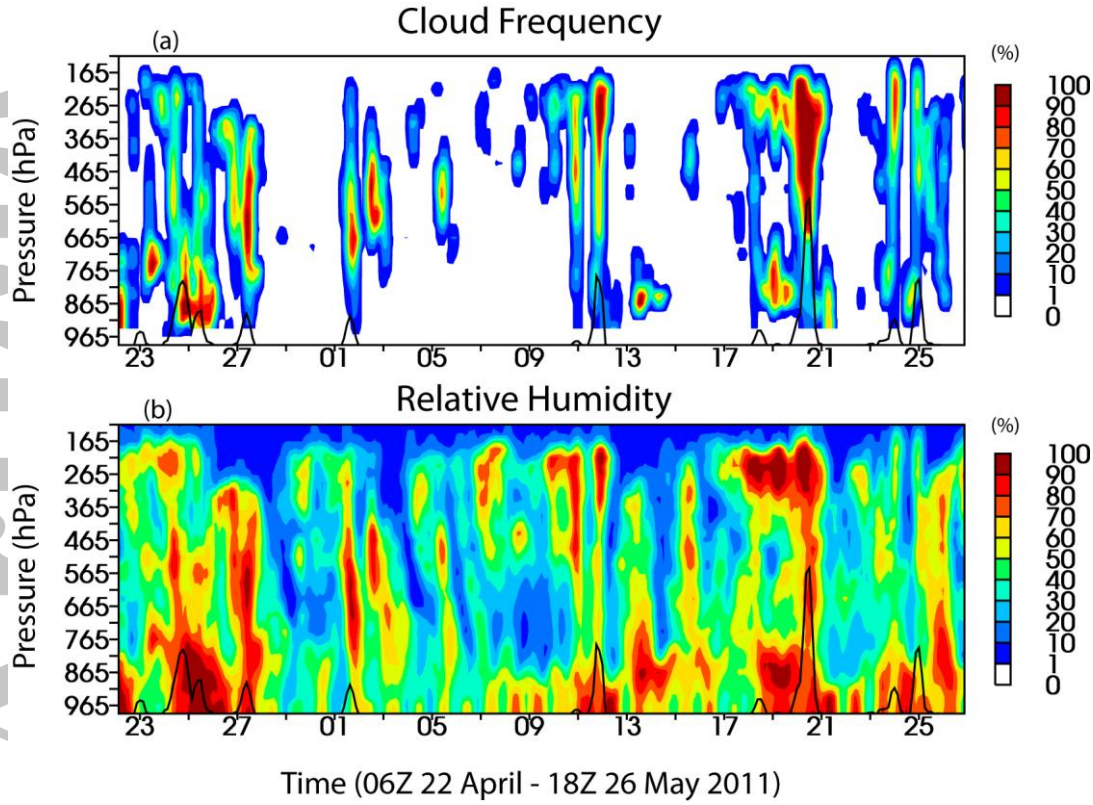

Figure 8. The time-pressure cross-sections of (a) cloud frequency of occurrence (%) at CF and (b) the analyzed relative humidity (with respect to ice for T < 00C) (%) over the analysis domain during MC3E. In these figures, black lines are surface precipitation rates. A 3-point running mean was applied to these fields for display purposes.

Accepted Article

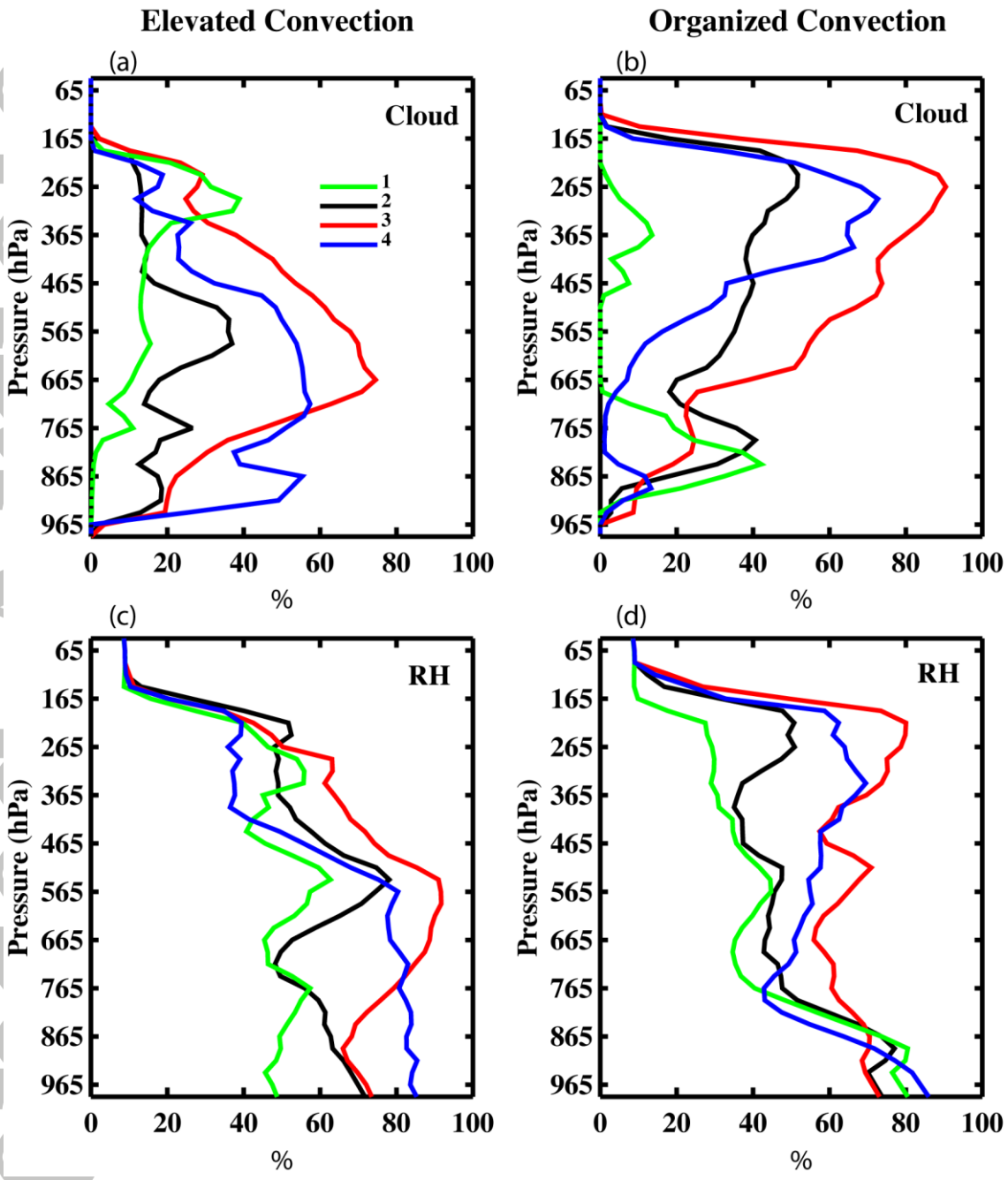

Figure 9. Composite profiles of cloud frequency of occurrence (upper panel) and relative humidity (lower panels) at different stages of convective systems. (a) and (c) Elevated convection; (b) and (d) Organized conveciton. The periods included in the average and the stages 1-4 are listed in Table 3.

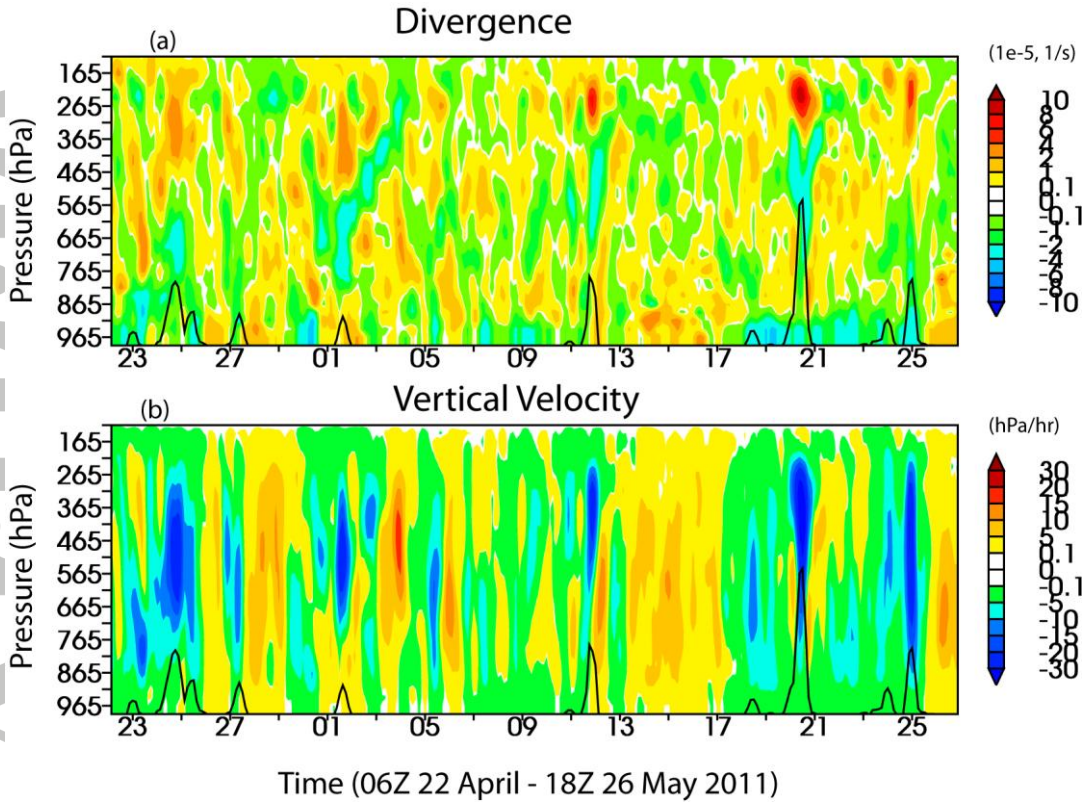

Figure 10. The time-pressure cross-sections of the analyzed (a) divergence (10-5, s-1) and vertical velocity (hPa hr-1) over the analysis domain during MC3E. In these figures, black lines are surface precipitation rates. A 3-point running mean was applied to these fields for display purposes.

Accepted Article

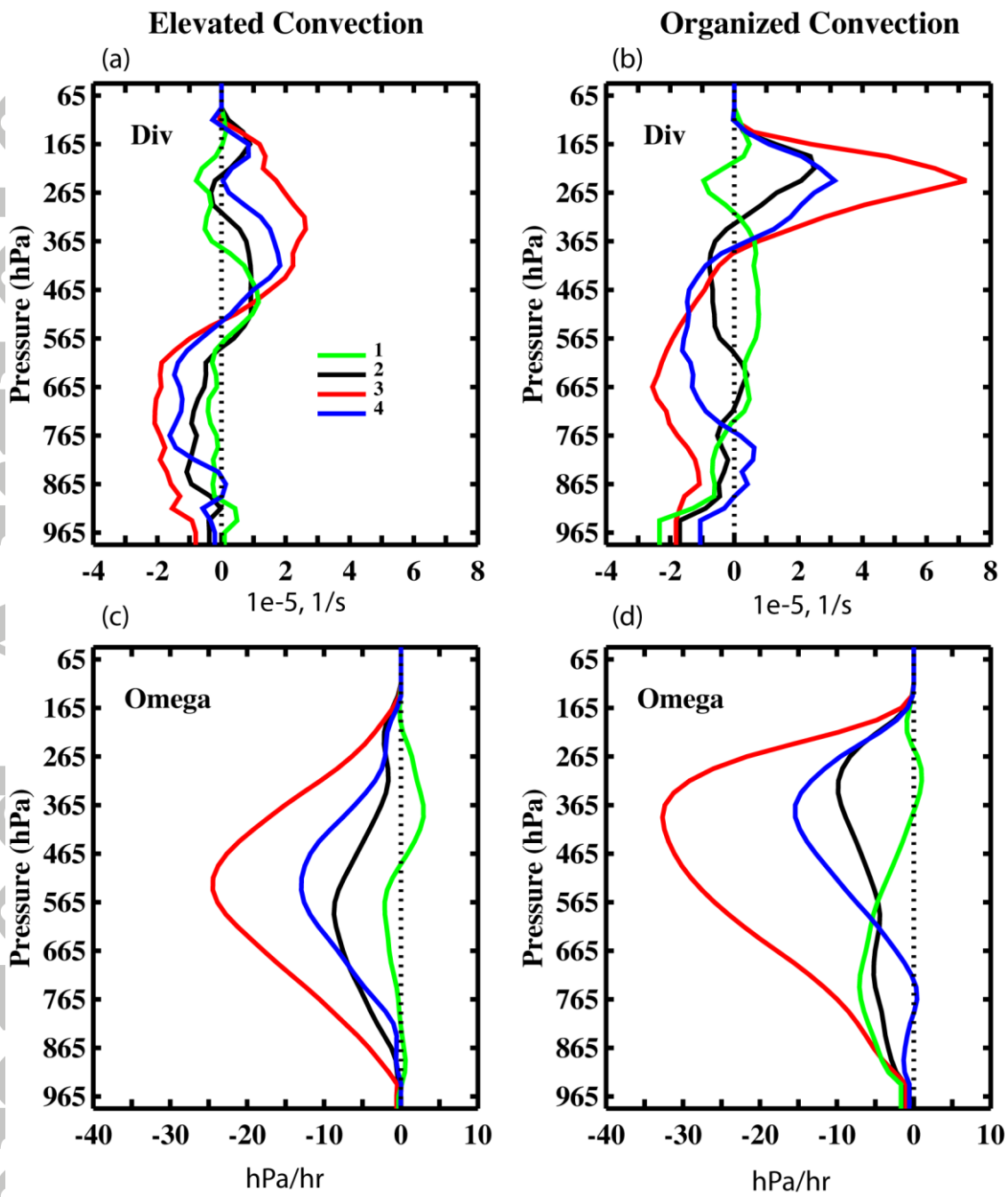

Figure 11. Composite profiles of divergence (upper panels) and vertical velocity (lower panels) at different stages of convective systems. (a) and (c) Elevated convection; (b) and (d) Organized convection. The periods included in the average and the stages 1-4 are listed in Table 3.

Accepted Article

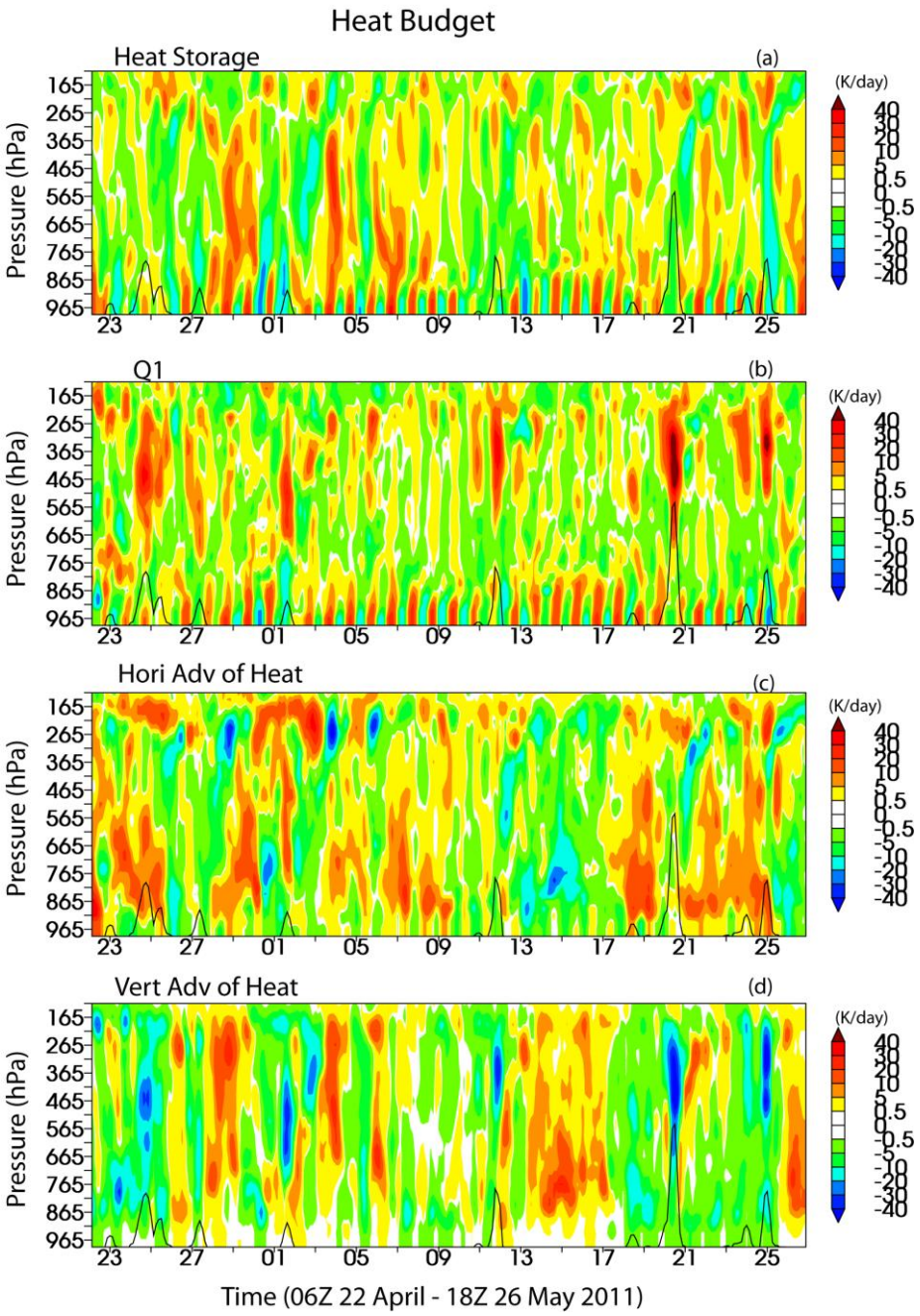

Figure 12. The time-pressure cross-sections of the analyzed heat budget terms over the analysis domain during MC3E. (a) Storage term; (b) Diabatic heating rate (Q1); (c) Horizontal advective tendency of temperature; and (d) Vertical advective tendency of temperature. Unit: K day-1. In these figures, black lines are surface precipitation rates. A 3-point running mean was applied to these fields for display purposes.

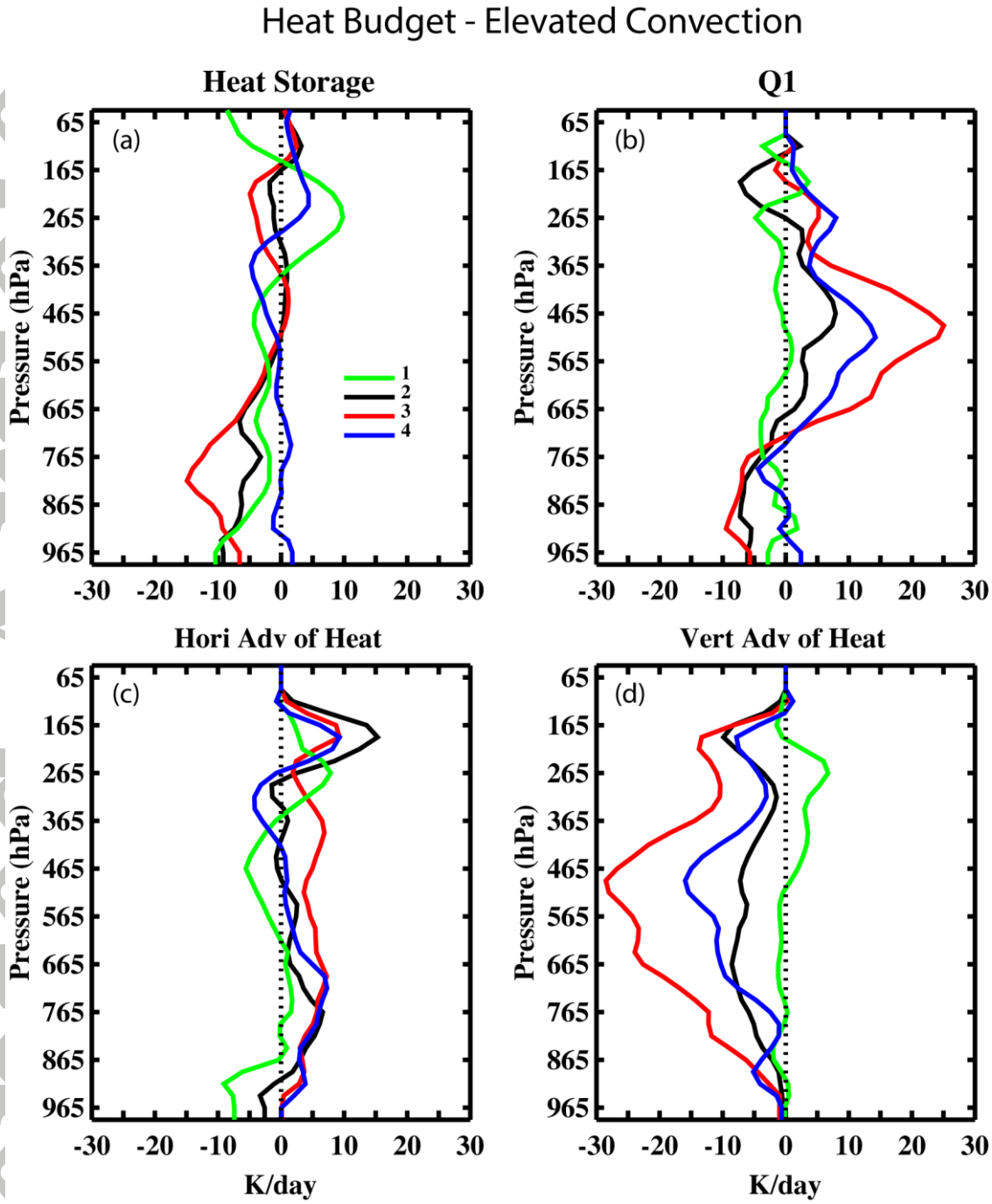

Figure 13. Composite profiles of heat budget terms at different stages (1-4) of elevated convective systems. (a) Storage term, (b) Q1, (c) Horizontal advective tendency of heat, and (d) Vertical advective tendency of heat. Units are K day^{-1}. The periods included in the average and the stages 1-4 are listed in Table 3.

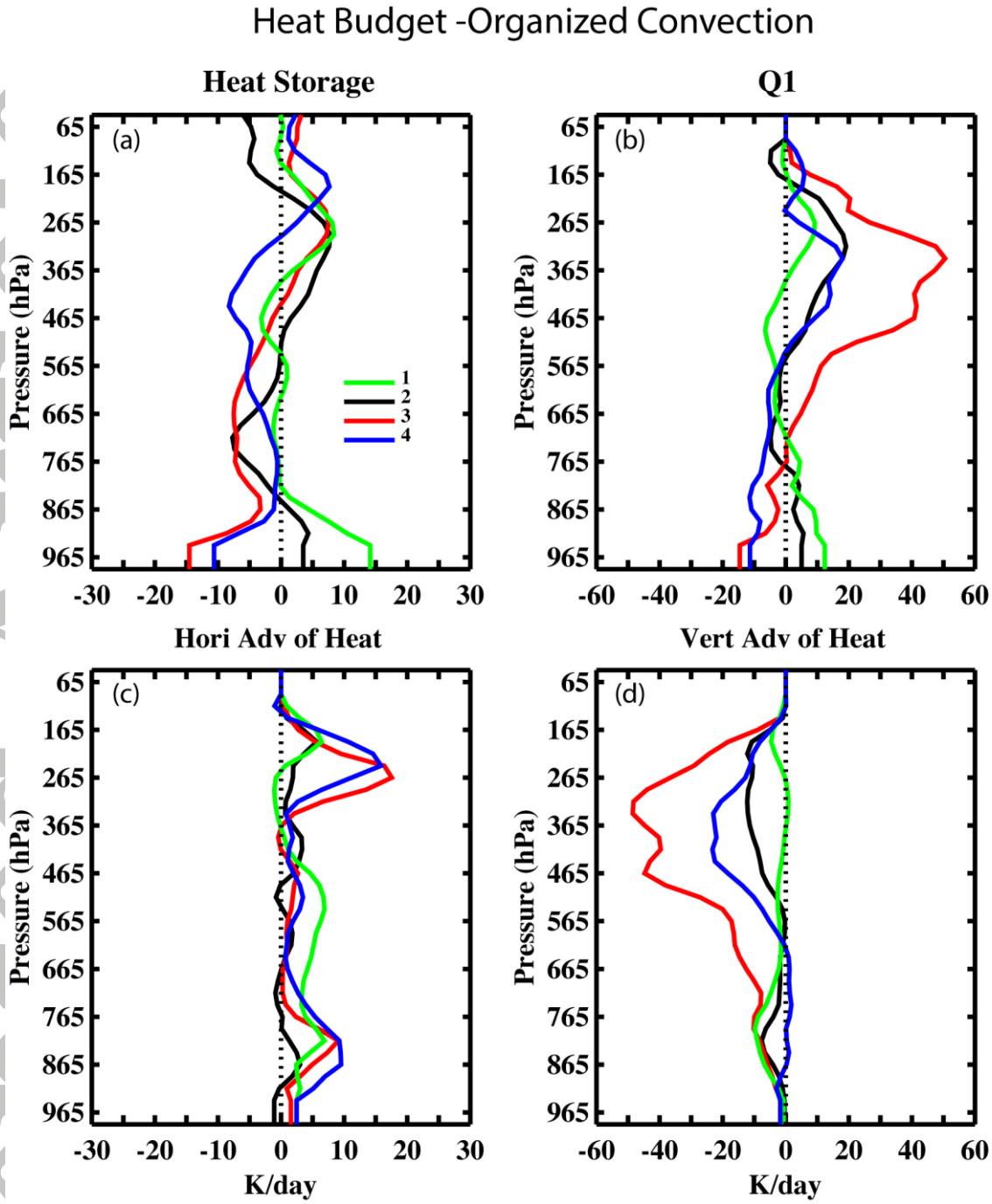

Figure 14. Same as Figure 13 except for organized convection.

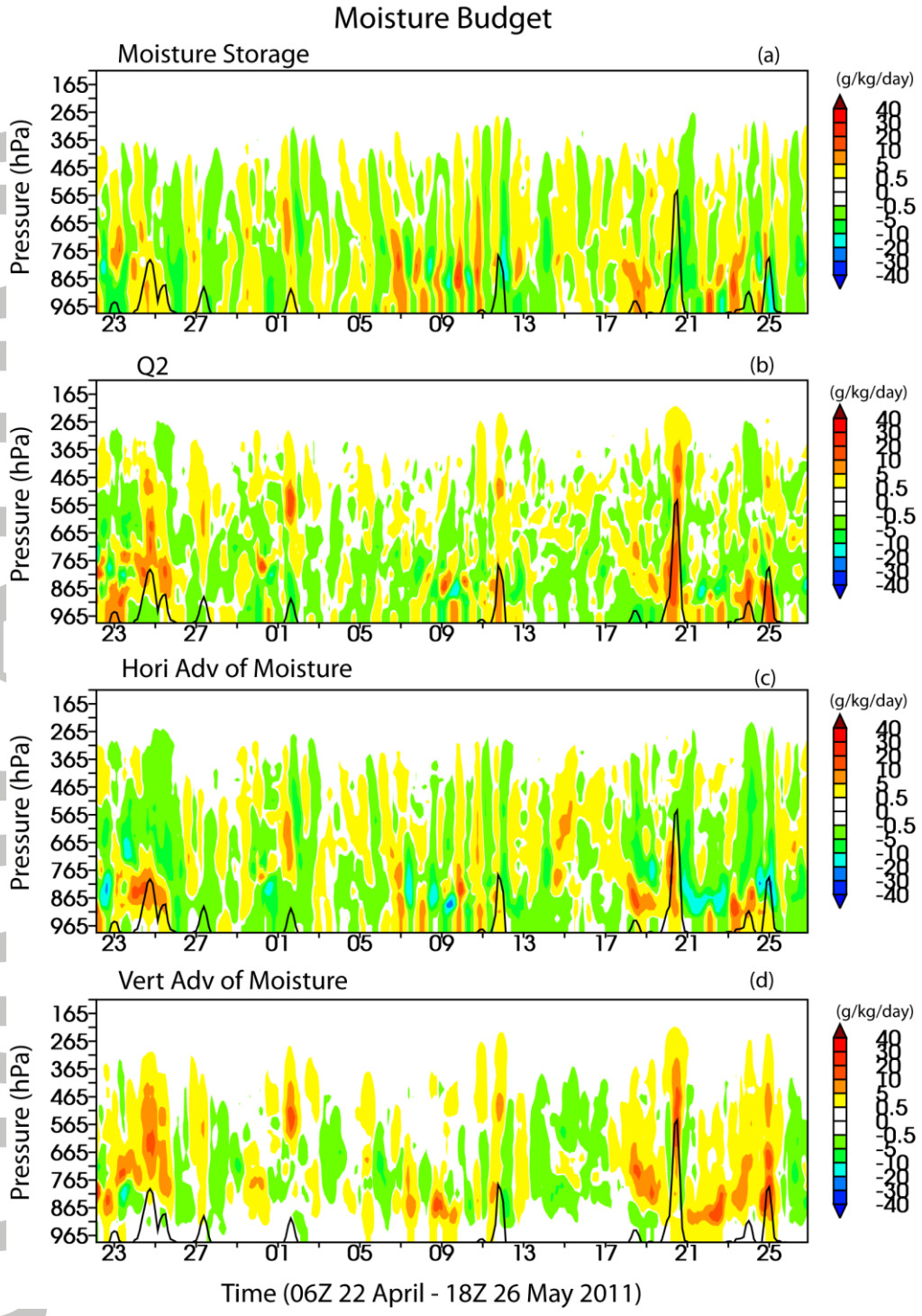

Figure 15. The time-pressure cross-sections of the analyzed moisture budget terms over the analysis domain during MC3E. (a) Storage term; (b) Diabatic drying rate (Q2); (c) Horizontal advective tendency of moisture; and (d) Vertical advective tendency of moisture. Unit: g kg-1 day-1. In these figures, black lines are surface precipitation rates. A 3-point running mean was applied to these fields for display purposes.

Accepted Article

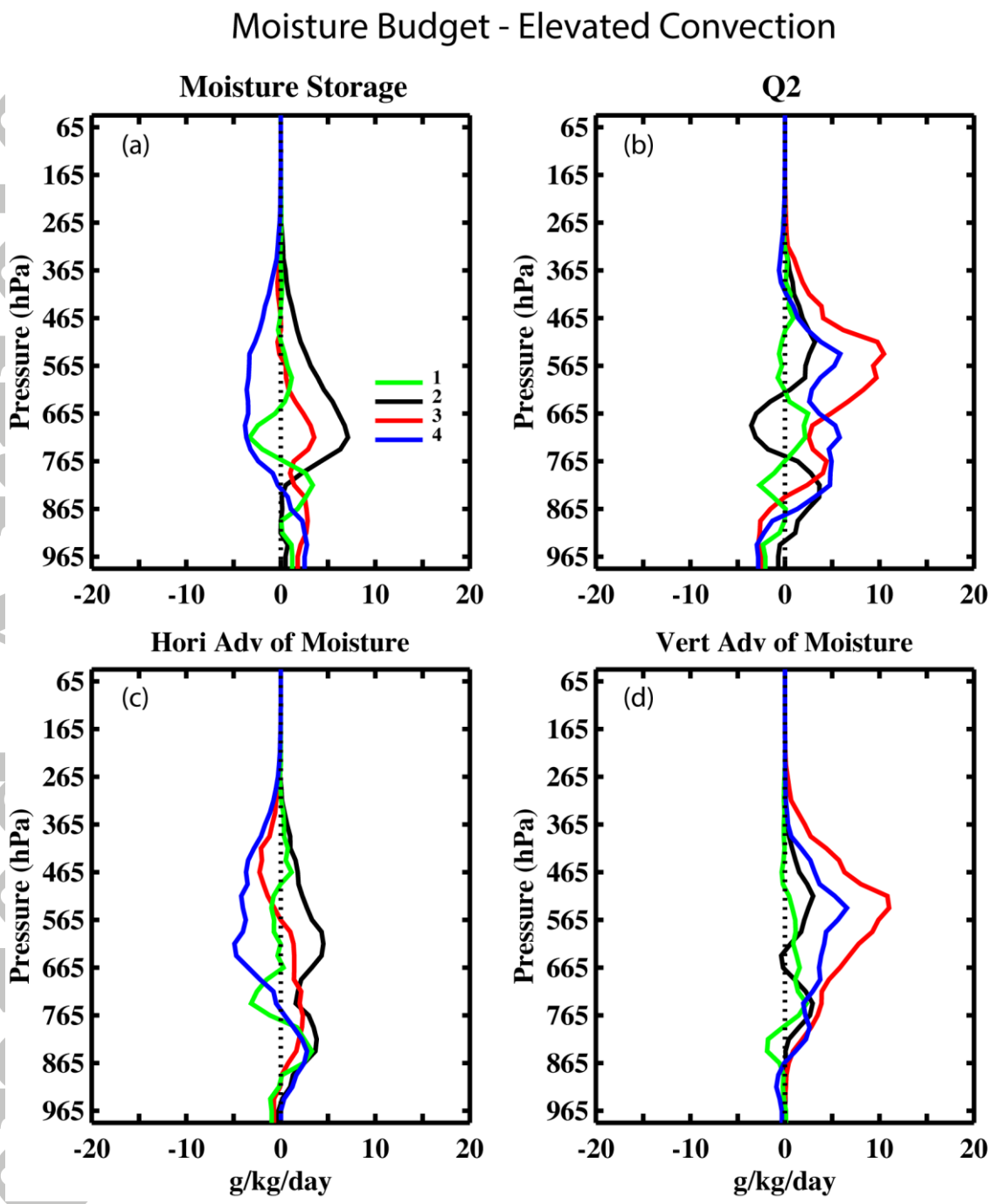

Figure 16. Same as Figure 13 except for moisture budget.

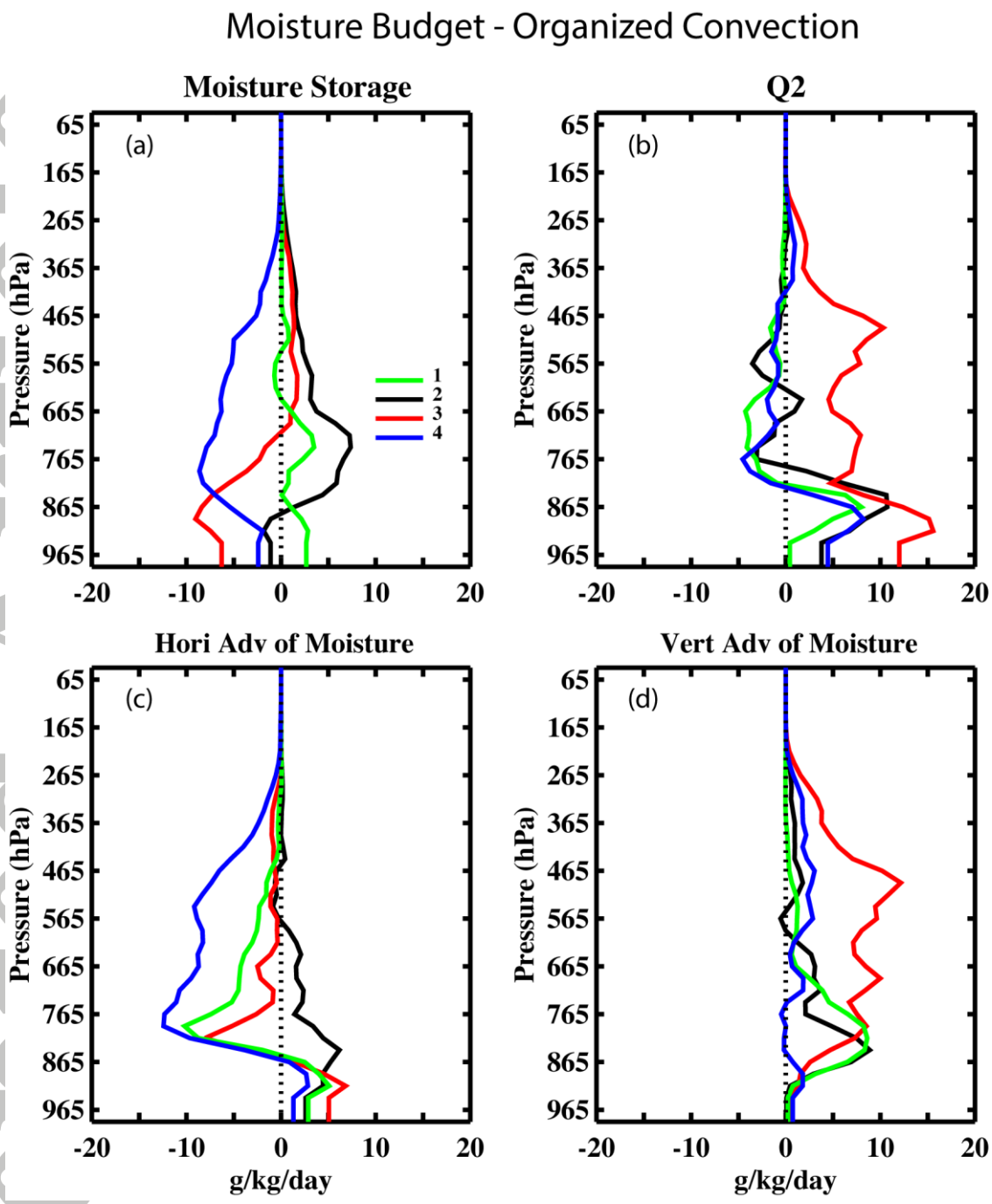

Figure 17. Same as Figure 14 except for moisture budget.

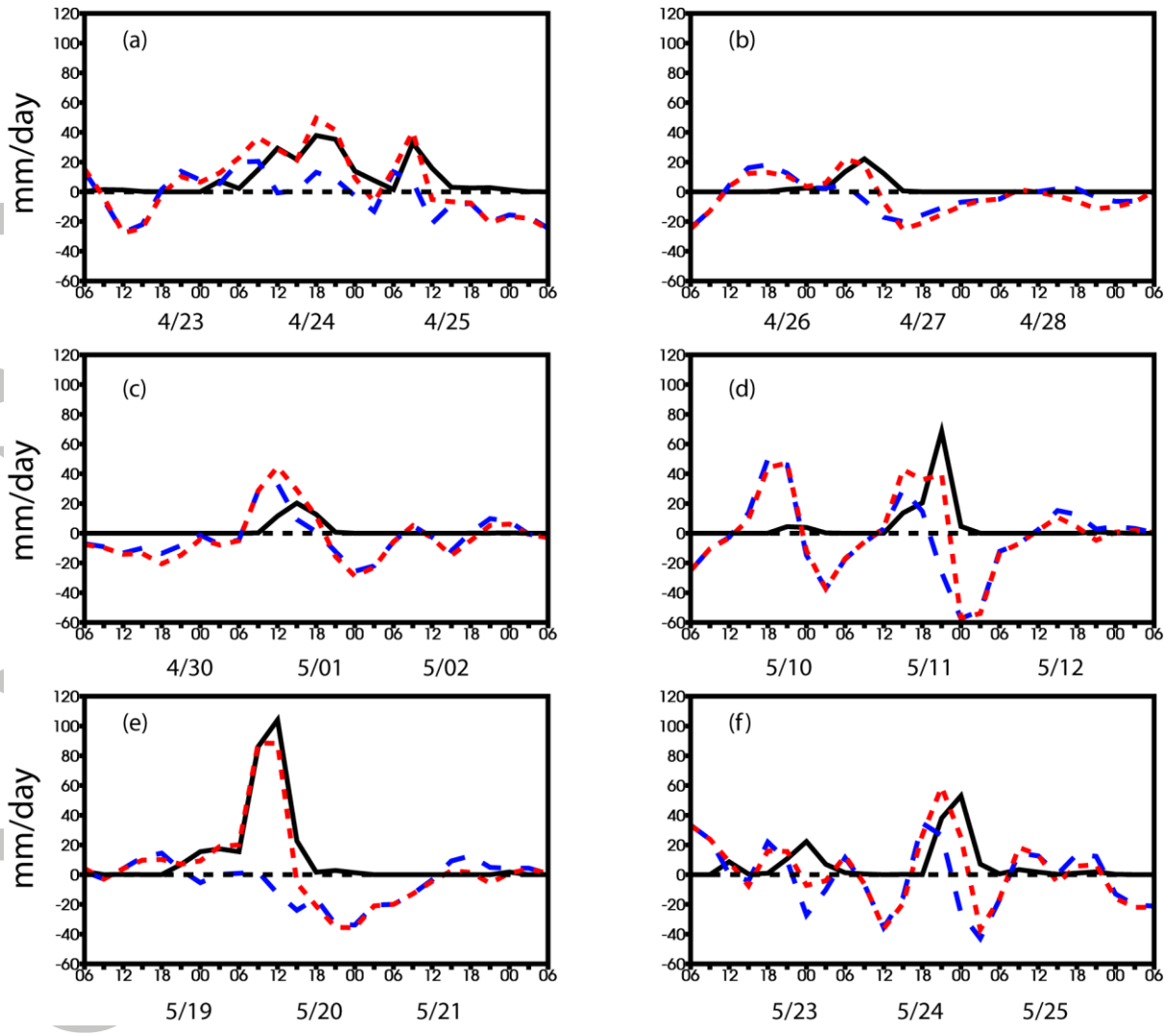

Figure 18. Precipitation rates (solid black) and vertically integrated moisture convergence (dashed-red) and storage term (long-dashed blue) averaged over the analysis domain for selected precipitation periods. Units are mm day-1. Time is UTC.

Accepted

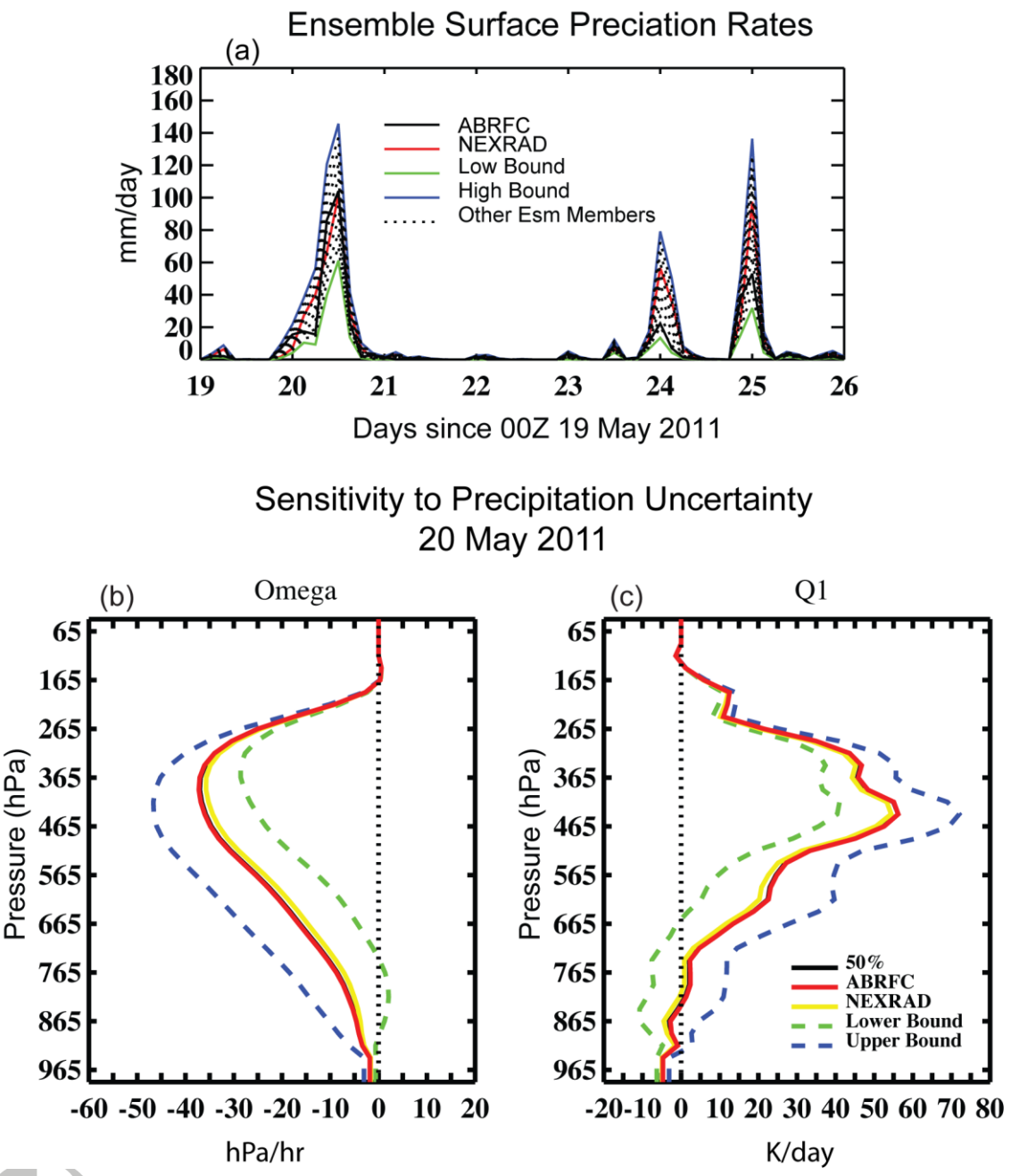

Figure 19. (a) Precipitation ensembles used in the analysis for a selected period of MC3E. Units are mm day-1. (b) Selected ensemble members of analyzed vertical velocity (hPa hr-1) and (c) Q1 (K day-1) averaged for the period between 09 Z - 15Z 20 May 2011 when a strong squall line propagated the experiment site.

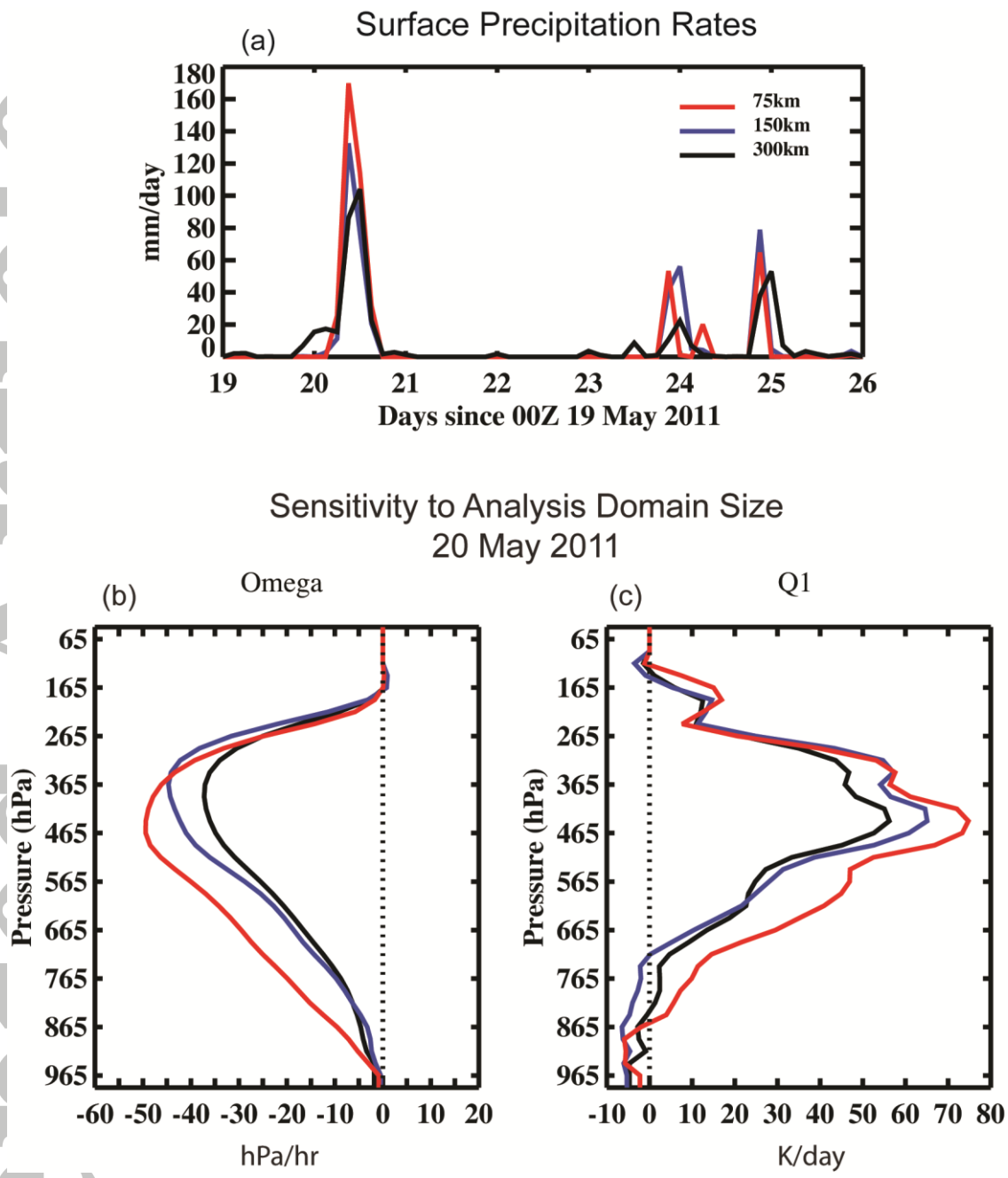

Figure 20. (a) Precipitation rates over different sizes of domain for a selected period of MC3E. Units are mm day-1. (b) Analyzed vertical velocity (hPa hr-1) and (c) Q1 (K day-1) over the three different sizes of domain averaged for the period between 09 Z - 15Z 20 May 2011 when a strong squall line propagated the experiment site.

Table 1. Required constraint variables in the variational analysis and their data sources.

Constraint Variables	**Data Sources**
Surface latent and sensible heat fluxes	Best-Estimate Fluxes from Energy Balance Bowen Ratio Measurements and Bulk Aerodynamics Calculations (BAEBBR)
Surface radiative fluxes	Data Quality Assessment for ARM Radiation Data (QCRAD)
Surface Precipitation	Arkansas-Red Basin River Forecast Center (ABRFC) 4-km rain gauge adjusted WSR-88D radar measurements and the bias-corrected National Severe Storm Laboratory (NSSL) National Mosaic and Multisensor Quantitative Precipitation Estimate (QPE) (NMQ) Next-Generation Radar (NEXRAD)-based precipitation
Surface Meteorology	Surface Meteorological Instrumentation (MET) Oklahoma Mesonet (OKM) Kansas State University Mesonet (KSU)
TOA radiative fluxes	GOES satellite retrieved SW/LW fluxes

Accepted Article

Table 2. Upper and lower bounds of the precipitation uncertainty range. P_a is the domain mean precipitation rate based on ABRFC, while P_n is the domain mean value from NEXRAD NMQ data.

Cases	Upper Bound	Lower Bound
$(P_a * P_n) \neq 0$	$\mathrm{Max}(P_a, P_n)*(1+0.4)$	$\mathrm{Min}(P_a, P_n)*(1-0.4)$
$(P_a * P_n) = 0$	$\mathrm{Max}(P_a, P_n)*(1+0.4)$	0

Accepted Article

Table 3. Classification of time periods for the selected scatter storms and squall lines. Local time in SGP is 5 hours less than universal time (Z).

	Scatter storms	Squall lines
Stage	Observation times	Observation times
1	00Z Apr 24, 00Z Apr 27, 06Z May 1	12Z May 11, 18Z May 19, 18Z May 23, 15Z May 24
2	09Z Apr 24, 06Z Apr 25, 03Z Apr 27, 09Z May 1	15Z May 11, 06Z May 20, 21Z May 23, 18Z May 24.
3	12Z Apr 24, 09Z Apr 25, 06Z Apr 27, 09Z Apr 27, 12Z May 1, 15Z May 1	18Z may 11, 21Z May 11, 12Z May 20, 00Z May 24, 21Z May 24, 00Z May 25
4	15Z Apr 24, 12Z Apr 25, 12Z Apr 27, 18Z May 1	00Z May 12, 18Z May 20, 03Z May 24, 03Z May 25

Accepted Article